RESEARCH ARTICLE

Efficient computation of the magnetic polarizabiltiy tensor spectral signature using proper orthogonal decomposition

Ben A. Wilson[1] | **Paul D. Ledger[2]**

[1]Zienkiewicz Centre for Computational Engineering, College of Engineering, Swansea University, Swansea, UK

[2]School of Computing & Mathematics, Keele University, Newcastle under Lyme, UK

Correspondence
P. D. Ledger, School of Computing & Mathematics, Keele University, Newcastle under Lyme, UK.

Funding information
Engineering and Physical Sciences Research Council, Grant/Award Number: EP/R002134/1

Abstract

The identification of hidden conducting permeable objects from measurements of the perturbed magnetic field taken over a range of low frequencies is important in metal detection. Applications include identifying threat items in security screening at transport hubs, location of unexploded ordnance, and antipersonnel landmines in areas of former conflict, searching for items of archeological significance and recycling of valuable metals. The solution of the inverse problem, or more generally locating and classifying objects, has attracted considerable attention recently using polarizability tensors. The magnetic polarizability tensor (MPT) provides a characterization of a conducting permeable object using a small number of coefficients, has an explicit formula for the calculation of their coefficients, and a well understood frequency behavior, which we call its spectral signature. However, to compute such signatures, and build a library of them for object classification, requires the repeated solution of a transmission problem, which is typically accomplished approximately using a finite element discretization. To reduce the computational cost, we propose an efficient reduced order model (ROM) that further reduces the problem using a proper orthogonal decomposition for the rapid computation of MPT spectral signatures. Our ROM benefits from a posteriori error estimates of the accuracy of the predicted MPT coefficients with respect to those obtained with finite element solutions. These estimates can be computed cheaply during the online stage of the ROM allowing the ROM prediction to be certified. To further increase the efficiency of the computation of the MPT spectral signature, we provide scaling results, which enable an immediate calculation of the signature under changes in the object size or conductivity. We illustrate our approach by application to a range of homogenous and inhomogeneous conducting permeable objects.

KEYWORDS

finite element method, magnetic polarizability tensor, metal detection, object characterization, reduced order model, spectral, validation

1 | INTRODUCTION

There is considerable interest in using the magnetic polarizability tensor (MPT) characterization of conducting permeable objects to classify and identify hidden targets in metal detection. The MPT is a complex symmetric rank 2 tensor, which has six independent coefficients, although the number of independent coefficients for objects with rotational or reflectional symmetries is smaller.[1] Its coefficients are a function of the exciting frequency, the object's size, its shape as well as its conductivity and permeability. Explicit formulas for computing the tensor coefficients have been derived[1-4] and validated against exact solutions and measurements.[3,5] Also, the way in which the tensor coefficients vary with the exciting frequency is theoretically well understood[4] offering improved object classification. The frequency (or spectral) behavior of the MPT is henceforth called its spectral signature.

In practical metal detection, the MPT coefficients can be determined from the perturbed magnetic field when a highly conducting object is placed in a low frequency time varying background field. The background field is generated by a set of *transmit coils* and the perturbed magnetic field is measured as a voltage in a set of *receive coils*. Systems of transmit and receive coils have been designed to carefully measure the spectral signature of the MPT in the laboratory[6,7] as well as for specific applications including walk through metal detectors at transport hubs,[8,9] the identification of antipersonnel landmines,[10] in-line scanning,[11,12] and the recycling of valuable metals.[13] Nevertheless, these systems will lead to noise and errors in the MPT coefficients. Errors may occur from a range of sources, including inaccuracies in the model used for the perturbed magnetic field and background field. The MPT object characterization has been shown to be associated with the leading order in an asymptotic expansion of the perturbed magnetic field as the object size goes to 0 and assumes the background field is uniform over the object.[1] In practice, this is not always the case and, if the object is placed in a highly nonuniform background, the higher order terms in the expansion may become important (and dominate) so that higher rank tensor characterizations of objects become important.[14] There will also be other errors and noise associated with capacitive coupling with low-conducting objects or soil in the background as well as general noise (e.g., from amplifiers, parasitic voltages in the receive coils and from filtering).[9] The amount of error and noise will vary from application to application and from system to system. For MPT spectral signatures obtained in laboratory the current accuracy is about 1% (e.g., Reference 7) while for walk through metal detectors it is about 5% (e.g., References 8,9), but the accuracy of these systems is improving all the time.

The MPT spectral signature has been exploited in a range of different classification algorithms including simple library classification for homogeneous[15] and inhomogeneous objects,[16] a k nearest neighbors (KNN) classification algorithm[8] and other machine learning approaches.[17] The MPT classification of objects has already been applied to a range of different applications including airport security screening,[8,18] waste sorting,[13] and antipersonnel landmine detection.[10] The aforementioned *supervised* classification techniques rely on a library of MPT spectral signatures to *learn* how to classify the objects. Previous practical applications have used libraries of measured MPT coefficients for known objects, relevant for the application under consideration, for example, Reference 9 considered between 3 and 13 classes of objects with up to 200 samples for the classification. But, such libraries are subject to errors and have unavoidable noise, as described above, and, hence, this may limit the performance of classification of unknown objects if it is then used in a metal detection system with less noise (and/or reduced errors) compared with the system used for the creating the training library. The purpose of this article is to describe an efficient tool for computing this library in order to overcome these challenges.

One approach for the automated computation of the MPT spectral signature is to postprocess finite element method (FEM) solutions to eddy current problems obtained using commercial packages (e.g., with ANSYS as in Reference 6); however, improved accuracy, and a better understanding, can be gained by using the available explicit expressions for MPT coefficients, which rely on computing finite element (FE) approximations to a transmission problem.[1,3,4] A further alternative would be to use the boundary element method (BEM) to discretize the transmission problem, which only requires discretization of the conductor's surface for a homogenous conductor and hence has fewer degrees of freedom. However, unlike the sparse matrices in FEM, BEM results in fully populated matrices, and, for general inhomogeneous objects, requires discretization of the conductor's volume and coupling with FEM. Appropriate types of BEM for the transmission problem are described in References 19,20. Nevertheless, to produce an accurate MPT spectral signature, the solution process (using FEM or BEM) must be repeated for a large number of excitation frequencies leading to potentially expensive computations for fine discretizations (with small mesh spacing and high order elements). The present article addresses this issue by proposing a reduced order model, in the form of a (projected) proper orthogonal decomposition (POD)

scheme, that relies on full order model solutions [1] computed using the established open source FE package, `NGSolve`, and the recently derived alternative explicit expressions formulas for the MPT coefficients.[4] The use of `NGSolve`[23,24] ensures that the solutions to underlying (eddy current type) transmission problems are accurately computed using high order $\boldsymbol{H}$(curl) conforming (high order edge element) discretizations (see References 25-27 and references therein) and the POD technique ensures their rapid computation over sweeps of frequency. This means the MPT coefficients are obtained with higher accuracy than can currently be achieved from measurements (noise appropriate to the system can be added to the library during a classifier training if desired), the spectral signature is accurately computed for a large frequency range (up to the limit of the eddy current model) rather than obtained at a small number of discrete frequencies and, through scripting, it allows a much larger library of objects and variations of materials to be considered, which is all highly desirable for achieving greater fidelity and accuracy when training machine learning classifiers.

Reduced order models (ROMs) based on POD have been successfully applied to efficiently generate solutions for new problem parameters using a small number representative full order model solutions (often called snapshots, e.g., References 21,22) in a range of engineering applications including mechanics,[28,29] thermal problems,[30,31] fluid flow[32,33] as well as electromagnetic problems with application to integrated circuits[34] and recently to coupled magnetomechanical problems.[22] However, ROMs have not been applied to the computation of MPT spectral signatures. A review of current POD techniques is provided in References 21,35.

The main novelty of the work is the application of a POD approach to the efficient and accurate computation of the MPT spectral signature and the derivation of a posteriori error estimates of the accuracy of reduced order predictions of the MPT coefficients with respect to those obtained with FEM. Importantly, these error estimates can be computed cheaply during the online stage of the ROM allowing the prediction of the MPT coefficients to be certified. This ROM approach is motivated by the previous success of POD approaches and the theoretical study,[4] which shows the spectral behavior of the MPT is characterized by a small number of functions and, hence, has a sparse representation. The practical computation requires only computing FE solution snapshots at a small number of frequencies and the evaluation of the MPT spectral signature follows from solving a series of extremely small linear systems. A second novelty is the presentation of simple scaling results, which enable the MPT spectral signature to easily be computed from an existing set of coefficients under the scaling of an object's conductivity or object size.

The article is organized as follows: Section 2 briefly reviews the eddy current model, which applies in metal detection, and the asymptotic expansion of the perturbed magnetic field in the presence of a conducting permeable object, which leads to the explicit expression of the MPT. Then, in Section 3, the FE model used for obtaining the full order model solutions is described. Section 4 presents the POD reduced order model scheme. This is followed, in Section 5, by the derivation of results that describe the scaling of the MPT under parameter changes. Sections 6 and 7 present numerical examples of the POD scheme for computing the frequency behavior of the MPT and examples of the scaling of the MPT under parameter changes, respectively.

2 | THE EDDY CURRENT MODEL AND ASYMPTOTIC EXPANSION

We briefly discuss the eddy current model along with stating the asymptotic expansion that forms the basis of the magnetic polarizability description of conducting objects in metal detection.

2.1 | Eddy current model

The eddy current model is a low frequency approximation of the Maxwell system that neglects the displacement currents, which is valid when the frequency is small and the conductivity of the body is high. A rigorous justification of the model involves the topology of the conducting body.[36] The eddy current model is described by the time-harmonic system

$$\nabla \times \boldsymbol{E}_\alpha = i\omega\mu\boldsymbol{H}_\alpha, \tag{1a}$$

$$\nabla \times \boldsymbol{H}_\alpha = \boldsymbol{J}_0 + \sigma\boldsymbol{E}_\alpha, \tag{1b}$$

---

[1] While there is some variation in literature, we follow References 21,22 and call the full order model that obtained by a discrete (e.g., FEM) approximation to a boundary value or transmission problem, which itself involves approximations.

where $\boldsymbol{E}_\alpha$ and $\boldsymbol{H}_\alpha$ are the electric and magnetic interaction fields, respectively, $\boldsymbol{J}_0$ is an external current source, $i := \sqrt{-1}$, ω is the angular frequency, μ is the magnetic permeability, and σ is the electric conductivity. We will use the eddy current model for describing the forward and inverse problems associated with metal detection.

2.1.1 | Forward problem

In the forward (or direct) problem, the position and materials of the conducting body B_α are known. The object has a high conductivity, $\sigma = \sigma_*$, and a permeability, $\mu = \mu_*$. For the purpose of this study, the conducting body is assumed to be buried in soil, which is assumed to be of a much lower conductivity so that $\sigma \approx 0$ and have a permeability $\mu = \mu_0 := 4\pi \times 10^{-7}$ H/m. A background field is generated by a solenoidal current source $\boldsymbol{J}_0$ with support in the air above the soil, which also has $\sigma = 0$ and $\mu = \mu_0$. As shown in Figure 1, the region around the object is $B_\alpha^c := \mathbb{R}^3 \setminus \overline{B_\alpha}$ where the overbar denotes the closure of B_α. We will also use the overbar to denote the complex conjugate, but it should be clear from the context as to which definition applies. Note that a similar model also applies in the situation of identifying hidden targets in security screening[8,18] and waste sorting[13] among others.

The forward model is described by the system (1), which holds in $\mathbb{R}^3$, with

$$\mu(\boldsymbol{x}) = \begin{cases} \mu_* & \boldsymbol{x} \in B_\alpha \\ \mu_0 & \boldsymbol{x} \in B_\alpha^c \end{cases}, \quad \sigma(\boldsymbol{x}) = \begin{cases} \sigma_* & \boldsymbol{x} \in B_\alpha \\ 0 & \boldsymbol{x} \in B_\alpha^c \end{cases}. \tag{2}$$

The regions B_α and B_α^c are coupled by the transmission conditions

$$[\boldsymbol{n} \times \boldsymbol{E}_\alpha]_{\Gamma_\alpha} = [\boldsymbol{n} \times \boldsymbol{H}_\alpha]_{\Gamma_\alpha} = \boldsymbol{0}, \tag{3}$$

which hold on $\Gamma_\alpha := \partial B_\alpha$. In the above, $[u]_{\Gamma_\alpha} := u|_+ - u|_-$ denotes the jump, the + refers to just outside of B_α, and the − to just inside and $\boldsymbol{n}$ denotes a unit outward normal to Γ_α.

The electric interaction field is nonphysical in B_α^c and, to ensure uniqueness of this field, the condition $\nabla \cdot \boldsymbol{E}_\alpha = 0$ is imposed in this region. Furthermore, we also require that $\boldsymbol{E}_\alpha = O(1/|\boldsymbol{x}|)$ and $\boldsymbol{H}_\alpha = O(1/|\boldsymbol{x}|)$ as $|\boldsymbol{x}| \to \infty$, denoting that the fields go to zero at least as fast as $1/|\boldsymbol{x}|$, although, in practice, this rate can be faster.

2.1.2 | Inverse problem

In metal detection, the inverse problem is to determine the location, shape and material properties (σ_* and μ_*) of the conducting object B_α from measurements of $(\boldsymbol{H}_\alpha - \boldsymbol{H}_0)(\boldsymbol{x})$ taken at a range of locations $\boldsymbol{x}$ in the air. As described in the introduction, there are considerable advantages in using spectral data, that is, additionally measuring $(\boldsymbol{H}_\alpha - \boldsymbol{H}_0)(\boldsymbol{x})$ over a range of frequencies ω, within the limit of the eddy current model. Here, $\boldsymbol{H}_0$ denotes the background magnetic field and $\boldsymbol{E}_0$ and $\boldsymbol{H}_0$ are the solutions of (1) with $\sigma = 0$ and $\mu = \mu_0$ in $\mathbb{R}^3$. Similar to above, we also require the decay conditions $\boldsymbol{E}_0 = O(1/|\boldsymbol{x}|)$ and $\boldsymbol{H}_0 = O(1/|\boldsymbol{x}|)$ as $|\boldsymbol{x}| \to \infty$. Note that practical metal detectors measure a voltage perturbation, which corresponds to $\int_S \boldsymbol{n} \cdot (\boldsymbol{H}_\alpha - \boldsymbol{H}_0)(\boldsymbol{x}) d\boldsymbol{x}$ over an appropriate surface S.[3] For very small coils, this voltage perturbation is approximated by $\boldsymbol{m} \cdot (\boldsymbol{H}_\alpha - \boldsymbol{H}_0)(\boldsymbol{x})$ where $\boldsymbol{m}$ is the magnetic dipole moment of the coil.[3]
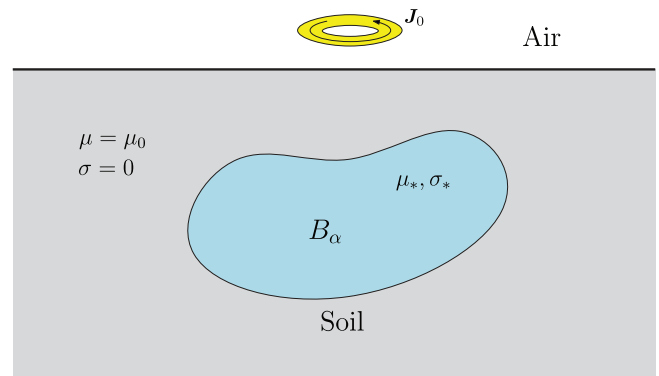
FIGURE 1 A diagram showing a hidden conducting object B_α, buried in soil, with a current source located in the air above

A traditional approach to the solution of this inverse problem involves creating a discrete set of voxels, each with unknown σ and μ, and posing the solution to the inverse problem as an optimization process in which σ and μ are found through minimization of an appropriate functional, for example, Reference 37. From the resulting images of σ and μ one then attempts to infer the shape and position of the object. However, this problem is highly ill-posed[38] and presents considerable challenges mathematically and computationally in the case of limited noisy measurement data.

Instead, we seek an approximation of the perturbation $(\boldsymbol{H}_\alpha - \boldsymbol{H}_0)(\boldsymbol{x})$ at some point $\boldsymbol{x}$ exterior to B_α, which allows objects to be characterized by a small number of coefficients in a MPT that are easily obtained from the measurements of $(\boldsymbol{H}_\alpha - \boldsymbol{H}_0)(\boldsymbol{x})$ once the object position is known, which can be found from a MUSIC algorithm, for example, Reference 2. The object identification then reduces to a classification problem, as discussed in the introduction.

2.2 | The asymptotic expansion and MPT description

Following References 1,2 we define $B_\alpha := \alpha B + \boldsymbol{z}$ where B is a unit size object with Lipschitz boundary, α is the object size and $\boldsymbol{z}$ is the object's translation from the origin as shown in Figure 2.

Then, using the asymptotic formula obtained by Ammari et al.,[2] Ledger and Lionheart[1] have derived the simplified form

$$(\boldsymbol{H}_\alpha - \boldsymbol{H}_0)(\boldsymbol{x})_i = (\boldsymbol{D}_x^2 G(\boldsymbol{x}, \boldsymbol{z}))_{ij}(\mathcal{M})_{jk}(\boldsymbol{H}_0(\boldsymbol{z}))_k + O(\alpha^4), \tag{4}$$

which holds as $\alpha \to 0$ and makes the MPT explicit. The relationship between the leading order term in the above to the dipole expansion of $(\boldsymbol{H}_\alpha - \boldsymbol{H}_0)(\boldsymbol{x})$ is discussed in Reference 3. In the above, $G(\boldsymbol{x}, \boldsymbol{z}) := 1/(4\pi|\boldsymbol{x} - \boldsymbol{z}|)$ is the free space Laplace Green's function, $\boldsymbol{D}_x^2 G$ denotes the Hessian of G and Einstein summation convention of the indices is implied. In addition, $\mathcal{M} = (\mathcal{M})_{jk}\boldsymbol{e}_j \otimes \boldsymbol{e}_k$, where $\boldsymbol{e}_i$ denotes the ith orthonormal unit vector, is the complex symmetric rank 2 MPT, which describes the shape and material properties of the object B_α and is frequency dependent, but is independent of the object's position $\boldsymbol{z}$, allowing the inverse problems of object location and object characterization to be separated. We will sometimes write $\mathcal{M}[\alpha B, \omega]$ to emphasize its dependence on αB and ω and also use $\mathcal{M}[\alpha B, \omega, \sigma_*, \mu_r]$ to emphasize its dependence also on $\mu_r := \mu_*/\mu_0$ and σ_*. The above formulation, and the definition of $\mathcal{M}$ below, are presented for the case of a single homogenous object B, the extension to multiple inhomogeneous objects can be found in References 4,16.

Using the derivation in Reference 4, we state the explicit formulas for the computation of the coefficients of $\mathcal{M}$, which are particularly well suited to a FEM discretization. The earlier explicit expressions in References 1,3,5 are equivalent for exact fields. We use the splitting $(\mathcal{M})_{ij} := (\mathcal{N}^0)_{ij} + (\mathcal{R})_{ij} + \mathrm{i}(\mathcal{I})_{ij}$ obtained in Reference 4 with
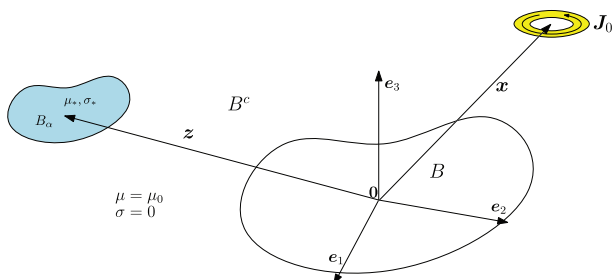
$$(\mathcal{N}^0[\alpha B])_{ij} := \alpha^3 \delta_{ij} \int_B (1 - \tilde{\mu}_r^{-1}) d\boldsymbol{\xi} + \frac{\alpha^3}{4} \int_{B \cup B^c} \tilde{\mu}_r^{-1} \nabla \times \tilde{\theta}_i^{(0)} \cdot \nabla \times \tilde{\theta}_j^{(0)} \, d\boldsymbol{\xi}, \tag{5a}$$

$$(\mathcal{R}[\alpha B, \omega])_{ij} := -\frac{\alpha^3}{4} \int_{B \cup B^c} \tilde{\mu}_r^{-1} \nabla \times \boldsymbol{\theta}_j^{(1)} \cdot \nabla \times \overline{\boldsymbol{\theta}_i^{(1)}} \, d\boldsymbol{\xi}, \tag{5b}$$

$$(\mathcal{I}[\alpha B, \omega])_{ij} := \frac{\alpha^3}{4} \int_B \nu \left(\boldsymbol{\theta}_j^{(1)} + \left(\tilde{\theta}_j^{(0)} + \boldsymbol{e}_j \times \boldsymbol{\xi} \right) \right) \cdot \overline{\left(\boldsymbol{\theta}_i^{(1)} + \left(\tilde{\theta}_i^{(0)} + \boldsymbol{e}_i \times \boldsymbol{\xi} \right) \right)} \, d\boldsymbol{\xi}, \tag{5c}$$

where $B^c := \mathbb{R}^3 \setminus \overline{B}$ and $\mathcal{N}^0[\alpha B]$, $\mathcal{R}[\alpha B, \omega]$, $\mathcal{I}[\alpha B, \omega]$ are real symmetric rank 2 tensors, which each have real eigenvalues. In the above, $\boldsymbol{\xi}$ is chosen to be measured from an origin inside B,

$$\tilde{\mu}_r(\boldsymbol{\xi}) := \begin{cases} \mu_r & \boldsymbol{\xi} \in B \\ 1 & \boldsymbol{\xi} \in B^c \end{cases},$$

FIGURE 2 A diagram showing the physical description of B_α with respect to the coordinate axes

and $v := \alpha^2 \omega \mu_0 \sigma_*$, δ_{ij} is the Kronecker delta. The computation of (5) rely on the real solution $\theta_i^{(0)}(\xi)$ of the transmission problem[4]

$$\nabla \times \tilde{\mu}_r^{-1} \nabla \times \theta_i^{(0)} = \mathbf{0} \quad \text{in } B \cup B^c, \tag{6a}$$

$$\nabla \cdot \theta_i^{(0)} = 0 \quad \text{in } B \cup B^c, \tag{6b}$$

$$\left[\mathbf{n} \times \theta_i^{(0)} \right]_\Gamma = \mathbf{0} \quad \text{on } \Gamma, \tag{6c}$$

$$\left[\mathbf{n} \times \tilde{\mu}_r^{-1} \nabla \times \theta_i^{(0)} \right]_\Gamma = \mathbf{0} \quad \text{on } \Gamma, \tag{6d}$$

$$\theta_i^{(0)} - \mathbf{e}_i \times \xi = \mathbf{O}\left(|\xi|^{-1}\right) \quad \text{as } |\xi| \to \infty, \tag{6e}$$

where $\Gamma := \partial B$ and the complex solution $\theta_i^{(1)}(\xi)$ of the transmission problem

$$\nabla \times \mu_r^{-1} \nabla \times \theta_i^{(1)} - \mathrm{i}v \left(\theta_i^{(0)} + \theta_i^{(1)} \right) = \mathbf{0} \quad \text{in } B, \tag{7a}$$

$$\nabla \times \nabla \times \theta_i^{(1)} = \mathbf{0} \quad \text{in } B^c, \tag{7b}$$

$$\nabla \cdot \theta_i^{(1)} = 0 \quad \text{in } B^c, \tag{7c}$$

$$\left[\mathbf{n} \times \theta_i^{(1)} \right]_\Gamma = \mathbf{0} \quad \text{on } \Gamma, \tag{7d}$$

$$\left[\mathbf{n} \times \tilde{\mu}_r^{-1} \nabla \times \theta_i^{(1)} \right]_\Gamma = \mathbf{0} \quad \text{on } \Gamma, \tag{7e}$$

$$\theta_i^{(1)} = \mathbf{O}\left(|\xi|^{-1}\right) \quad \text{as } |\xi| \to \infty. \tag{7f}$$

Note also that we choose to introduce $\tilde{\theta}_i^{(0)}(\xi) := \theta_i^{(0)}(\xi) - \mathbf{e}_i \times \xi$, which can be shown to satisfy the same transmission problem as (6) except with a nonzero jump condition for $\left[\mathbf{n} \times \tilde{\mu}_r^{-1} \nabla \times \tilde{\theta}_i^{(0)} \right]_\Gamma$ and the decay condition $\tilde{\theta}_i^{(0)}(\xi) = \mathbf{O}\left(|\xi|^{-1}\right)$ as $|\xi| \to \infty$.

3 | FULL ORDER MODEL

To approximate the solutions to the transmission problems (6) and (7) we truncate the unbounded domain B^c at a finite distance from the object B and create a bounded domain Ω containing B. On $\partial\Omega$, we approximate the decay conditions (6e) and (7f) by $\mathbf{n} \times \tilde{\theta}_i^{(0)} = \mathbf{n} \times \left(\theta_i^{(0)} - \mathbf{e}_i \times \xi \right) = \mathbf{0}$ and $\mathbf{n} \times \theta_i^{(1)} = \mathbf{0}$, respectively. On this finite domain, we approximate the associated weak variational statements to these problems using FEM with a $\mathbf{H}(\text{curl})$ conforming discretization with mesh spacing h and order elements p where

$$\mathbf{H}(\text{curl}) := \{\mathbf{u} : \mathbf{u} \in \left(L^2(\Omega)\right)^3, \ \nabla \times \mathbf{u} \in \left(L^2(\Omega)\right)^3\}, \tag{8}$$

and $L^2(\Omega)$ denotes the standard space of square integrable functions. In Section 3.1 we provide their weak formulations and provide their discretization in Section 3.2. It is clear that the eddy current model (1), the asymptotic formula (4), the domain truncation to form Ω and the steps that follow to form a discrete FE model all involve approximations. However, our goal is to accurately and efficiently obtain the MPT coefficients in (5) and, to distinguish the coefficients obtained using FEM from those obtained from the further reduced ROM, we call their FEM approximation the full order model.

3.1 | Weak formulation of the problem

Following the approach advocated in Reference 25 for magnetostatic and eddy current problems, we add a regularization term $\varepsilon \int_\Omega \tilde{\theta}_i^{(0)} \cdot \psi d\xi$, where ε is a small regularization parameter, to the weak variational statement of (6), written in terms

of $\tilde{\theta}_i^{(0)}$, in order to circumvent the Coulomb gauge $\nabla \cdot \tilde{\theta}_i^{(0)} = 0$. For details of the small error induced by this approximation see References 25, 27. Then, by choosing an appropriate set of $\boldsymbol{H}$(curl) conforming finite element functions in $W^{(hp)} \subset \boldsymbol{H}$(curl), we obtain the following discrete regularized weak form for (6) : Find real solutions $\tilde{\theta}_i^{(0,hp)} \in Y \cap W^{(hp)}$ such that

$$
\int_\Omega \tilde{\mu}_r^{-1} \nabla \times \tilde{\theta}_i^{(0,hp)} \cdot \nabla \times \boldsymbol{\psi}^{(hp)} d\boldsymbol{\xi} + \varepsilon \int_\Omega \tilde{\theta}_i^{(0,hp)} \cdot \boldsymbol{\psi}^{(hp)} d\boldsymbol{\xi}
$$
$$
= 2 \int_B \left(1 - \mu_r^{-1}\right) \boldsymbol{e}_i \cdot \nabla \times \boldsymbol{\psi}^{(hp)} d\boldsymbol{\xi}, \tag{9}
$$

for all $\boldsymbol{\psi}^{(hp)} \in Y \cap W^{(hp)}$, where

$$
Y := \{\boldsymbol{u} \in \boldsymbol{H}(\text{curl}) : \boldsymbol{n} \times \boldsymbol{u} = \boldsymbol{0} \text{ on } \partial\Omega\}.
$$

In a similar manner, the discrete weak variational statement of (7) is: Find complex solutions $\theta_i^{(1,hp)} \in Y \cap W^{(hp)}$ such that

$$
\int_\Omega \left(\mu_r^{-1} \nabla \times \theta_i^{(1,hp)}\right) \cdot \left(\nabla \times \overline{\boldsymbol{\psi}^{(hp)}}\right) d\boldsymbol{\xi} - i \int_B \nu \theta_i^{(1,hp)} \cdot \overline{\boldsymbol{\psi}^{(hp)}} d\boldsymbol{\xi}
$$
$$
+ \varepsilon \int_{\Omega \backslash B} \theta_i^{(1,hp)} \cdot \overline{\boldsymbol{\psi}^{(hp)}} d\boldsymbol{\xi} = i \int_B \nu \theta_i^{(0,hp)} \cdot \overline{\boldsymbol{\psi}^{(hp)}} d\boldsymbol{\xi}, \tag{10}
$$

for all $\boldsymbol{\psi}^{(hp)} \in Y \cap W^{(hp)}$.

For what follows it is beneficial to restate (10) in the following form: Find $\theta_i^{(1,hp)} \in Y \cap W^{(hp)}$ such that

$$
a\left(\theta_i^{(1,hp)}, \boldsymbol{\psi}^{(hp)}; \boldsymbol{\omega}\right) = r\left(\boldsymbol{\psi}^{(hp)}; \theta_i^{(0,hp)}, \boldsymbol{\omega}\right), \tag{11}
$$

for all $\boldsymbol{\psi}^{(hp)} \in Y \cap W^{(hp)}$ where

$$
a\left(\theta_i^{(1,hp)}, \boldsymbol{\psi}^{(hp)}; \boldsymbol{\omega}\right) := \left\langle \tilde{\mu}^{-1} \nabla \times \theta_i^{(1,hp)}, \nabla \times \boldsymbol{\psi}^{(hp)} \right\rangle_{L^2(\Omega)}
$$
$$
- i \left\langle \nu \theta_i^{(1,hp)}, \boldsymbol{\psi}^{(hp)} \right\rangle_{L^2(B)}
$$
$$
+ \varepsilon \left\langle \theta_i^{(1,hp)}, \boldsymbol{\psi}^{(hp)} \right\rangle_{L^2(\Omega \backslash B)}, \tag{12a}
$$
$$
r\left(\boldsymbol{\psi}^{(hp)}; \theta_i^{(0,hp)}, \boldsymbol{\omega}\right) := i \left\langle \nu \theta_i^{(0,hp)}, \boldsymbol{\psi}^{(hp)} \right\rangle_{L^2(B)}, \tag{12b}
$$

$\langle \boldsymbol{u}, \boldsymbol{v} \rangle_{L^2(\Omega)} := \int_\Omega \boldsymbol{u} \cdot \overline{\boldsymbol{v}} d\boldsymbol{\xi}$ denotes the L^2 inner product over Ω and $\boldsymbol{\omega}$ indicates the list of the problem parameters $(\omega, \sigma_*, \mu_r, \alpha)$ that one might wish to vary. Note that $r\left(\boldsymbol{\psi}^{(hp)}; \theta_i^{(0,hp)}, \boldsymbol{\omega}\right)$ is a function of μ_r as $\theta_i^{(0,hp)}$ depends on μ_r.

3.2 | Finite element discretization

For the implementation of (9) and (11), we use NGSolve[23,24,27,39] along with the hierarchic set of $\boldsymbol{H}$(curl) conforming basis functions proposed by Schöberl and Zaglmayr,[26] which are available in this software. In the following, for simplicity, we focus on the treatment of $\theta_i^{(1,hp)}$ and drop the index i as each direction can be computed in a similar way (as can $\tilde{\theta}_i^{(0,hp)}$). We denote these basis functions by $\boldsymbol{N}^{(k)}(\boldsymbol{\xi}) \in W^{(hp)}$ leading to the expression of the solution function along with the weighting functions

$$
\theta^{(1,hp)}(\boldsymbol{\xi}, \boldsymbol{\omega}) := \sum_{k=1}^{N_d} \boldsymbol{N}^{(k)}(\boldsymbol{\xi}) q_k(\boldsymbol{\omega}), \tag{13a}
$$
$$
\boldsymbol{\psi}^{(hp)}(\boldsymbol{\xi}, \boldsymbol{\omega}) := \sum_{k=1}^{N_d} \boldsymbol{N}^{(k)}(\boldsymbol{\xi}) l_k(\boldsymbol{\omega}), \tag{13b}
$$

where N_d is the number of degrees of freedom. Here, and in the following, the bold italic font denotes a vector field and the bold nonitalic Roman font represents a matrix (upper case) or column vector (lower case). With this distinction, we rewrite (13) in matrix form as

$$\boldsymbol{\theta}^{(1,hp)}(\boldsymbol{\xi},\boldsymbol{\omega}) = \mathbf{N}(\boldsymbol{\xi})\,\mathbf{q}(\boldsymbol{\omega}),\tag{14a}$$

$$\boldsymbol{\psi}^{(hp)}(\boldsymbol{\xi},\boldsymbol{\omega}) = \mathbf{N}(\boldsymbol{\xi})\,\mathbf{l}(\boldsymbol{\omega}),\tag{14b}$$

where $\mathbf{N}(\boldsymbol{\xi})$ is the matrix constructed with the basis vectors $\boldsymbol{N}^k(\boldsymbol{\xi})$ as its columns, that is,

$$\mathbf{N}(\boldsymbol{\xi}) := \left[\boldsymbol{N}^{(1)}(\boldsymbol{\xi}),\boldsymbol{N}^{(2)}(\boldsymbol{\xi}),...,\boldsymbol{N}^{(N_d)}(\boldsymbol{\xi})\right].$$

With this, we may also rewrite (11) as follows

$$\sum_{i=1}^{N_d}\sum_{j=1}^{N_d}\overline{l_i(\boldsymbol{\omega})}a\left(\boldsymbol{N}^{(j)}(\boldsymbol{\xi}),\boldsymbol{N}^{(i)}(\boldsymbol{\xi});\boldsymbol{\omega}\right)q_j(\boldsymbol{\omega}) = \sum_{i=1}^{N_d}\overline{l_i(\boldsymbol{\omega})}r\left(\boldsymbol{N}^{(i)}(\boldsymbol{\xi});\boldsymbol{\theta}^{(0,hp)},\boldsymbol{\omega}\right),\tag{15}$$

and, with a suitable choice of $l_i(\boldsymbol{\omega})$, we may rewrite (15) as the linear system of equations

$$\mathbf{A}(\boldsymbol{\omega})\,\mathbf{q}(\boldsymbol{\omega}) = \mathbf{r}\left(\boldsymbol{\theta}^{(0,hp)},\boldsymbol{\omega}\right),\tag{16}$$

where the coefficients of $\mathbf{A}(\boldsymbol{\omega})$ and $\mathbf{r}\left(\boldsymbol{\theta}^{(0,hp)},\boldsymbol{\omega}\right)$ are defined to be

$$(\mathbf{A}(\boldsymbol{\omega}))_{ij} := a\left(\boldsymbol{N}^{(j)}(\boldsymbol{\xi}),\boldsymbol{N}^{(i)}(\boldsymbol{\xi});\boldsymbol{\omega}\right),\tag{17a}$$

$$\left(\mathbf{r}\left(\boldsymbol{\theta}^{(0,hp)},\boldsymbol{\omega}\right)\right)_i := r\left(\boldsymbol{N}^{(i)}(\boldsymbol{\xi});\boldsymbol{\theta}^{(0,hp)},\boldsymbol{\omega}\right).\tag{17b}$$

`NGSolve` offers efficient approaches for the computational solution to (16) using preconditioned iterative solvers,[25,27] which we exploit. Following the solution of (16), we can obtain $\boldsymbol{\theta}^{(1,hp)}(\boldsymbol{\xi},\boldsymbol{\omega})$ using (14) and, by repeating the process for $i = 1, 2, 3$, we get $\boldsymbol{\theta}_i^{(1,hp)}(\boldsymbol{\xi},\boldsymbol{\omega})$. Then $(\mathcal{M}[\alpha B,\omega])_{ij}$, for the full order model, is found by using (5).

4 | REDUCED ORDER MODEL (ROM)

A traditional (full order model) approach for the computation of the MPT spectral signature, that is, the variation of the coefficients of $\mathcal{M}[\alpha B,\omega]$ with frequency, would involve the repeated solution of the N_d sized system (16) for different ω. To reduce the computational cost of this, we wish to apply a ROM in which the solution of (16) is replaced by a surrogate problem of reduced size. Thus, reducing both the computation cost and time to produce a solution for each new ω. In particular, in Section 4.1, we describe a ROM based on the POD method[21,22,35,40] and, in Section 4.2, apply the variant called projection based POD (which we denote by PODP), which has already been shown to work well in the analysis of magnetomechanical coupling applied to MRI scanners.[22] To emphasize the generality of the approach, the formulation is presented for an arbitrary list of problem parameters denoted by $\boldsymbol{\omega}$. In Section 4.3 we derive a procedure for computing certificates of accuracy on the ROM solutions with negligible additional cost.

4.1 | Proper orthogonal decomposition

Following the solution of (16) for $\mathbf{q}(\boldsymbol{\omega})$ for different values of the set of parameters, $\boldsymbol{\omega}$, we construct a matrix $\mathbf{D} \in \mathbb{C}^{N_d \times N}$ with the vector of solution coefficients as its columns in the form

$$\mathbf{D} := \left[\mathbf{q}(\boldsymbol{\omega}_1),\mathbf{q}(\boldsymbol{\omega}_2),...,\mathbf{q}(\boldsymbol{\omega}_N)\right].\tag{18}$$

Note that $\mathbf{q}(\boldsymbol{\omega}_i)$ denotes the vector of coefficients, which, when combined with (14a), produces a representative full order model solution snapshot for the ith set of parameters $\boldsymbol{\omega}_i$ and $N \ll N_d$ denotes the number of such snapshots. Application of a singular value decomposition (SVD), for example, References 41-43 gives

$$\mathbf{D} = \mathbf{U}\boldsymbol{\Sigma}\mathbf{V}^H, \tag{19}$$

where $\mathbf{U} \in \mathbb{C}^{N_d \times N_d}$ and $\mathbf{V} \in \mathbb{C}^{N \times N}$ are unitary matrices and $\boldsymbol{\Sigma} \in \mathbb{R}^{N_d \times N}$ is a diagonal matrix enlarged by zeros so that it becomes rectangular. In the above, $\mathbf{V}^H = \overline{\mathbf{V}}^T$ is the Hermitian of $\mathbf{V}$.

The diagonal entries $(\boldsymbol{\Sigma})_{ii} = \sigma_i^2$ are the singular values of $\mathbf{D}$ and they are arranged as $\sigma_1 > \sigma_2 > \ldots > \sigma_N$. Based on the sparse representation of the solutions to (7) as function of ν, and hence ω, (and hence also the sparse representation of the MPT) found in Reference 4, we expect these to decay rapidly toward zero, which motivates the introduction of a truncated singular value decomposition (TSVD), for example, References 41,42

$$\mathbf{D} \approx \mathbf{D}^M = \mathbf{U}^M \boldsymbol{\Sigma}^M (\mathbf{V}^M)^H, \tag{20}$$

where $\mathbf{U}^M \in \mathbb{C}^{N_d \times M}$ are the first M columns of $\mathbf{U}$, $\boldsymbol{\Sigma}^M \in \mathbb{R}^{M \times M}$ is a diagonal matrix containing the first M singular values and $(\mathbf{V}^M)^H \in \mathbb{C}^{M \times N}$ are the first M rows of $\mathbf{V}^H$. The computation of (20) constitutes the offline stage of the POD. Using (20) we can recover an approximate representation for each of our solution snapshots as follows

$$\mathbf{q}(\boldsymbol{\omega}_j) \approx \mathbf{U}^M \boldsymbol{\Sigma}^M \left((\mathbf{V}^M)^H \right)_j, \tag{21}$$

where $((\mathbf{V}^M)^H)_j$ refers to the jth column of $(\mathbf{V}^M)^H$.

4.2 | Projection-based proper orthogonal decomposition (PODP)

In the online stage of PODP, $\mathbf{q}^{\text{PODP}}(\boldsymbol{\omega}) \approx \mathbf{q}(\boldsymbol{\omega})$ is obtained by taking a linear combination of the columns of $\mathbf{U}^M$ where the coefficients of this projection are contained in the vector $\mathbf{p}^M(\boldsymbol{\omega})$. We choose to also approximate $\mathbf{l}(\boldsymbol{\omega})$ in a similar way so that

$$\theta^{(1,hp)}(\boldsymbol{\xi}, \boldsymbol{\omega}) \approx \left(\theta^{(1,hp)}\right)^{\text{PODP}}(\boldsymbol{\xi}, \boldsymbol{\omega}) := \mathbf{N}(\boldsymbol{\xi})\mathbf{q}^{\text{PODP}}(\boldsymbol{\omega}) = \mathbf{N}(\boldsymbol{\xi})\mathbf{U}^M\mathbf{p}^M(\boldsymbol{\omega}) \in Y^{(\text{PODP})}, \tag{22a}$$

$$\boldsymbol{\psi}^{(hp)}(\boldsymbol{\xi}, \boldsymbol{\omega}) \approx \left(\boldsymbol{\psi}^{(1,hp)}\right)^{\text{PODP}}(\boldsymbol{\xi}, \boldsymbol{\omega}) := \mathbf{N}(\boldsymbol{\xi})\mathbf{l}^{\text{PODP}}(\boldsymbol{\omega}) = \mathbf{N}(\boldsymbol{\xi})\mathbf{U}^M\mathbf{o}^M(\boldsymbol{\omega}) \in Y^{(\text{PODP})}, \tag{22b}$$

where $Y^{(\text{PODP})} \subset Y \cap W^{(hp)}$. Substituting these lower dimensional representations into (15) we obtain the following

$$\sum_{i=1}^{M}\sum_{j=1}^{M} \overline{o_i^M(\boldsymbol{\omega})} a(\mathbf{N}^{(j)}(\boldsymbol{\xi})(\mathbf{U}^M)_j, \mathbf{N}^{(i)}(\boldsymbol{\xi})(\mathbf{U}^M)_i; \boldsymbol{\omega}) p_j^M(\boldsymbol{\omega})$$

$$= \sum_{i=1}^{M} \overline{o_i^M(\boldsymbol{\omega})} r(\mathbf{N}^{(i)}(\boldsymbol{\xi})(\mathbf{U}^M)_i; \theta^{(0,hp)}, \boldsymbol{\omega})$$

$$(\mathbf{o}^M(\boldsymbol{\omega}))^H((\mathbf{U}^M)^H\mathbf{A}(\boldsymbol{\omega})\mathbf{U}^M)\mathbf{p}^M(\boldsymbol{\omega}) = (\mathbf{o}^M(\boldsymbol{\omega}))^H(\mathbf{U}^M)^H\mathbf{r}(\theta^{(0,hp)}, \boldsymbol{\omega}). \tag{23}$$

Then, if we choose $\mathbf{o}^M(\boldsymbol{\omega})$ appropriately, we obtain the linear system

$$\mathbf{A}^M(\boldsymbol{\omega})\mathbf{p}^M(\boldsymbol{\omega}) = \mathbf{r}^M\left(\theta^{(0,hp)}, \boldsymbol{\omega}\right), \tag{24}$$

which is of size $M \times M$ where $\mathbf{A}^M(\boldsymbol{\omega}) := (\mathbf{U}^M)^H \mathbf{A}(\boldsymbol{\omega})\mathbf{U}^M$ and $\mathbf{r}^M\left(\theta^{(0,hp)}, \boldsymbol{\omega}\right) := (\mathbf{U}^M)^H\mathbf{r}\left(\theta^{(0,hp)}, \boldsymbol{\omega}\right)$. Note, since $M < N \ll N_d$, this is significantly smaller than (16) and, therefore, substantially computationally cheaper to solve. After solving this reduced system, and obtaining $\mathbf{p}^M(\boldsymbol{\omega})$, we obtain an approximate solution for $\theta^{(1,hp)}(\boldsymbol{\xi}, \boldsymbol{\omega})$ using (22).

---

[2]Note that σ_* is used for conductivity and σ_i for a singular value; however, it should be clear from the application as to which definition applies.

Focusing on the particular case where $\boldsymbol{\omega} = \omega$, from (12) we observe that we can express $\mathbf{A}$ and $\mathbf{r}$ as the simple sums

$$\mathbf{A}(\omega) = \mathbf{A}^{(0)} + \omega \mathbf{A}^{(1)},$$

$$\mathbf{r}\left(\theta^{(0,hp)}, \omega\right) = \omega \mathbf{r}^{(1)}\left(\theta^{(0,hp)}\right),$$

where the definitions of $\mathbf{A}^{(0)}$, $\mathbf{A}^{(1)}$, and $\mathbf{r}^{(1)}\left(\theta^{(0,hp)}\right)$ are obvious from (17), (12), and the definition of ν. Then, by computing and storing $(\mathbf{U}^M)^H \mathbf{A}^{(0)} \mathbf{U}^M$, $(\mathbf{U}^M)^H \mathbf{A}^{(1)} \mathbf{U}^M$, $\left(\mathbf{U}^M\right)^H \mathbf{r}^{(1)}\left(\theta^{(0,hp)}\right)$, which are independent of ω, it follows that $\mathbf{A}^M(\omega)$ and $\mathbf{r}^M\left(\theta^{(0,hp)}, \omega\right)$ can be efficiently calculated for each new ω from the stored data. In a similar manner, by precomputing appropriate data, the MPT coefficients in (5) can also be rapidly evaluated for each new ω using the PODP solutions. This leads to further considerable computational savings. We emphasize that the PODP is only applied to obtain ROM solutions for $\theta^{(1)}(\xi, \omega)$ and not to $\theta^{(0)}(\xi)$, which does not depend on ω.

4.3 | An a posteriori error estimate to certify the PODP output

We follow the approach described in Reference 21, which enables us to derive an a posteriori error estimate on the MPT coefficients obtained with PODP, with respect to those obtained with full order model, as a function of ω. Importantly, this estimate can be computed at negligible additional cost during the online stage of PODP allowing it to be used to certify the MPT coefficients obtained using the ROM and to check their accuracy is within acceptable limits. To do this, we set $\varepsilon_i(\omega) = \theta_i^{(1,hp)}(\omega) - \left(\theta_i^{(1,hp)}\right)^{\mathrm{PODP}}(\omega) \in Y^{(hp)}$, where we have reintroduced the subscript i, as we need to distinguish between the cases $i = 1, 2, 3$. Although ε_i also depends on ξ, we have chosen here, and in the following, to only emphasize its dependence on ω. We have also introduced $Y^{(hp)} = Y \cap W^{(hp)}$ for simplicity of notation, and note that this error satisfies

$$a\left(\varepsilon_i(\omega), \psi; \omega\right) = r\left(\psi; \theta_i^{(0,hp)}, \omega\right) \qquad \forall \psi \in Y^{(hp)}, \tag{25}$$

which is called the error equation[21] and

$$a\left(\varepsilon_i(\omega), \psi; \omega\right) = 0 \qquad \forall \psi \in Y^{(\mathrm{PODP})}, \tag{26}$$

which is called Galerkin orthogonality.[21] The Riesz representation[21] of $r\left(\cdot; \theta_i^{(0,hp)}, \omega\right)$ denoted by $\hat{r}_i(\omega) \in Y^{(hp)}$ is such that

$$\left(\hat{r}_i(\omega), \psi\right)_{Y^{(hp)}} = r\left(\psi; \theta_i^{(0,hp)}, \omega\right) \qquad \forall \psi \in Y^{(hp)}, \tag{27}$$

so that

$$a\left(\varepsilon_i(\omega), \psi; \omega\right) = \left(\hat{r}_i(\omega), \psi\right)_{Y^{(hp)}} \qquad \forall \psi \in Y^{(hp)}. \tag{28}$$

Then, by using the alternative set of formulas for the tensor coefficients[4]

$$\left(\mathcal{R}[\alpha B, \omega]\right)_{ij} = -\frac{\alpha^3}{4} \int_B \nu \mathrm{Im}\left(\theta_j^{(1,hp)}\right) \cdot \theta_i^{(0,hp)} d\xi = -\frac{\alpha^3}{4} \left\langle \nu \mathrm{Im}\left(\theta_j^{(1,hp)}\right), \theta_i^{(0,hp)} \right\rangle_{L^2(B)}, \tag{29a}$$

$$\left(\mathcal{I}[\alpha B, \omega]\right)_{ij} = \frac{\alpha^3}{4} \left(\int_B \nu \mathrm{Re}\left(\theta_j^{(1,hp)}\right) \cdot \theta_i^{(0,hp)} d\xi + \int_B \nu \theta_j^{(0,hp)} \cdot \theta_i^{(0,hp)} d\xi \right)$$

$$= \frac{\alpha^3}{4} \left(\left\langle \nu \mathrm{Re}\left(\theta_j^{(1,hp)}\right), \theta_i^{(0,hp)} \right\rangle_{L^2(B)} + \left\langle \nu \theta_j^{(0,hp)}, \theta_i^{(0,hp)} \right\rangle_{L^2(B)} \right), \tag{29b}$$

which are written in terms of the full order solutions, we obtain an a posteriori error estimate for the tensor entries computed using PODP stated in the lemma below. Note that the formulae stated in (5) are used for the actual POD computation of $\left(\mathcal{R}^{\mathrm{PODP}}[\alpha B, \omega]\right)_{ij}$ and $\left(\mathcal{I}^{\mathrm{PODP}}[\alpha B, \omega]\right)_{ij}$, but the form in (29) is useful for obtaining the error estimate. Also, as $\left(\mathcal{N}[\alpha B]\right)_{ij}$ is independent of ω we have $\left(\mathcal{N}^{0,\mathrm{PODP}}[\alpha B]\right)_{ij} = \left(\mathcal{N}^0[\alpha B]\right)_{ij}$ and we write $\mathcal{M}^{\mathrm{PODP}}[\alpha B, \omega] = \mathcal{N}^{0,\mathrm{PODP}}[\alpha B] + \mathcal{R}^{\mathrm{PODP}}[\alpha B, \omega] + i\mathcal{I}^{\mathrm{PODP}}[\alpha B, \omega]$ for the MPT obtained by PODP.

Lemma 1. *An a posteriori error estimate for the tensor coefficients computed using PODP is*

$$|(\mathcal{R}[\alpha B, \omega])_{ij} - (\mathcal{R}^{\text{PODP}}[\alpha B, \omega])_{ij}| \leq (\Delta[\omega])_{ij}, \tag{30a}$$

$$|(\mathcal{I}[\alpha B, \omega])_{ij} - (\mathcal{I}^{\text{PODP}}[\alpha B, \omega])_{ij}| \leq (\Delta[\omega])_{ij}, \tag{30b}$$

where

$$(\Delta[\omega])_{ij} := \frac{\alpha^3}{8\alpha_{LB}} \left(\|\hat{r}_i(\omega)\|^2_{Y^{(hp)}} + \|\hat{r}_j(\omega)\|^2_{Y^{(hp)}} + \|\hat{r}_i(\omega) - \hat{r}_j(\omega)\|^2_{Y^{(hp)}} \right),$$

and α_{LB} is a lower bound on a stability constant.

Proof. We concentrate on the proof for $|(\mathcal{R}[\alpha B, \omega])_{ij} - (\mathcal{R}^{\text{PODP}}[\alpha B, \omega])_{ij}|$ as the proof for the second bound is similar and leads to the same result. Recalling the symmetry of $\mathcal{R}[\alpha B, \omega]$, we have $(\mathcal{R}[\alpha B, \omega])_{ij} = \frac{1}{2}((\mathcal{R}[\alpha B, \omega])_{ij} + (\mathcal{R}[\alpha B, \omega])_{ji})$ so that

$$
\begin{aligned}
D := |(\mathcal{R}[\alpha B, \omega])_{ij} - (\mathcal{R}^{\text{PODP}}[\alpha B, \omega])_{ij}| &= \frac{\alpha^3}{8} \left| \left\langle v\text{Im}(\epsilon_i), \theta_j^{(0,hp)} \right\rangle_{L^2(B)} + \left\langle v\text{Im}(\epsilon_j), \theta_i^{(0,hp)} \right\rangle_{L^2(B)} \right| \\
&= \frac{\alpha^3}{8} \left| \left\langle v\text{Im}(\epsilon_i), \theta_i^{(0,hp)} \right\rangle_{L^2(B)} + \left\langle v\text{Im}(\epsilon_i), \theta_j^{(0,hp)} - \theta_i^{(0,hp)} \right\rangle_{L^2(B)} \right. \\
&\quad \left. + \left\langle v\text{Im}(\epsilon_j), \theta_j^{(0,hp)} \right\rangle_{L^2(B)} + \left\langle v\text{Im}(\epsilon_j), \theta_i^{(0,hp)} - \theta_j^{(0,hp)} \right\rangle_{L^2(B)} \right| \\
&= \frac{\alpha^3}{8} \left| \left\langle v\text{Im}(\epsilon_i), \theta_i^{(0,hp)} \right\rangle_{L^2(B)} + \left\langle v\text{Im}(\epsilon_i - \epsilon_j), \theta_j^{(0,hp)} - \theta_i^{(0,hp)} \right\rangle_{L^2(B)} \right. \\
&\quad \left. + \left\langle v\text{Im}(\epsilon_j), \theta_j^{(0,hp)} \right\rangle_{L^2(B)} \right|,
\end{aligned}
$$

which follows since v and $\theta_i^{(0,hp)}$ are real valued and where we have dropped the dependence of ω on ϵ_i for simplicity of presentation. Thus,

$$D \leq \frac{\alpha^3}{8} \left(\left| \left\langle v\epsilon_i, \theta_i^{(0,hp)} \right\rangle_{L^2(B)} \right| + \left| \left\langle v(\epsilon_i - \epsilon_j), \theta_j^{(0,hp)} - \theta_i^{(0,hp)} \right\rangle_{L^2(B)} \right| + \left| \left\langle v\epsilon_j, \theta_j^{(0,hp)} \right\rangle_{L^2(B)} \right| \right).$$

Next, using (25), we make the observation that

$$\left| \left\langle v\epsilon_i, \theta_i^{(0,hp)} \right\rangle_{L^2(B)} \right| = \left| r\left(\epsilon_i; \theta_i^{(0,hp)}, \omega\right) \right| = \left| a(\epsilon_i, \epsilon_i; \omega) \right| = \|\epsilon_i\|^2_\omega.$$

Also, since $r\left(\psi; \theta_j^{(0,hp)} - \theta_i^{(0,hp)}, \omega\right) = a\left(\theta_j^{(1,hp)}(\omega) - \theta_i^{(1,hp)}(\omega), \psi; \omega\right) = a(\epsilon_j - \epsilon_i, \psi; \omega)$ for all $\psi \in Y^{(hp)}$, we have $\left| \left\langle v\psi, \theta_j^{(0,hp)} - \theta_i^{(0,hp)} \right\rangle_{L^2(B)} \right| = \left| a(\epsilon_j - \epsilon_i, \psi; \omega) \right|$ so that

$$\left| \left\langle v(\epsilon_i - \epsilon_j), \theta_j^{(0,hp)} - \theta_i^{(0,hp)} \right\rangle_{L^2(B)} \right| = \left| r\left(\epsilon_i - \epsilon_j; \theta_j^{(0,hp)} - \theta_i^{(0,hp)}, \omega\right) \right| = |a(\epsilon_j - \epsilon_i, \epsilon_i - \epsilon_j; \omega)| = \|\epsilon_i - \epsilon_j\|^2_\omega,$$

and, hence,

$$D \leq \frac{\alpha^3}{8}(\|\epsilon_i\|^2_\omega + \|\epsilon_i - \epsilon_j\|^2_\omega + \|\epsilon_j\|^2_\omega). \tag{31}$$

Following similar steps to [21, pp. 47–50], and introducing a Riesz representation in (27), we can find that

$$\|\epsilon_i\|^2_\omega \leq \frac{\|\hat{r}_i(\omega)\|^2_{Y^{(hp)}}}{\alpha_{LB}}, \qquad \|\epsilon_j\|^2_\omega \leq \frac{\|\hat{r}_j(\omega)\|^2_{Y^{(hp)}}}{\alpha_{LB}}, \qquad \|\epsilon_i - \epsilon_j\|^2_\omega \leq \frac{\|\hat{r}_i(\omega) - \hat{r}_j(\omega)\|^2_{Y^{(hp)}}}{\alpha_{LB}},$$

and, combining this with (31), completes the proof. ∎

Remark 1. The a posteriori error estimate in Lemma 1 allow the coefficients of $\mathcal{M}^{\text{PODP}}[\alpha B, \omega]$ obtained by PODP to be certified at low-computational cost during the on-line stage of the ROM using the procedure described below. The bound does not give an explicit dependence on N or ω, but, if desired, could be used as part of an iterative procedure to choose additional candidate ω values for the representative full order model solution snapshots in a similar manner to that described in Reference 21. The (spectral) behavior $\mathcal{M}[\alpha B, \omega]$ with ω has been considered in Reference 4, where results on the functions that characterize the spectral signature of the MPT are provided.

The efficient evaluation of (30) follows the approach presented in [21, pp. 52–54], adapted to complex matrices and with the simplification that we compute a Riesz representation $\hat{\boldsymbol{r}}_i(\omega) \in Y^{(h0)}$ using lowest order elements for computational efficiency. The computations are split in to those performed in the offline stage and those in the on-line stage as follows.

In the offline stage, the following $(2M+1) \times (2M+1)$ Hermitian matrices are computed

$$\mathbf{G}^{(i,j)} = \left(\mathbf{W}^{(i)}\right)^H \mathbf{M}_0^{-1} \mathbf{W}^{(j)},$$

where, since $\mathbf{G}^{(j,i)} = (\mathbf{G}^{(i,j)})^H$, it follows that, in practice, only the three matrices $\mathbf{G}^{(1,1)}$, $\mathbf{G}^{(2,2)}$, and $\mathbf{G}^{(3,3)}$ are required for computing the certificates on the diagonal entries of the tensors, and the further three matrices $\mathbf{G}^{(1,2)}$, $\mathbf{G}^{(1,3)}$, and $\mathbf{G}^{(2,3)}$ are needed for the off-diagonal terms. In the above, $(\mathbf{M}_0)_{ij} = \langle \boldsymbol{N}^{(i)}, \boldsymbol{N}^{(j)} \rangle_{L^2(\Omega)}$ are the coefficients of a real symmetric FEM mass matrix for the lowest order, with $\boldsymbol{N}^{(i)}, \boldsymbol{N}^{(j)} \in W^{(h0)}$ being typical lowest order basis functions, and

$$\mathbf{W}^{(i)} := \mathbf{P}_0^p \left(\mathbf{r}^{(1)}\left(\boldsymbol{\theta}_i^{(0)}\right) \quad \mathbf{A}^{(0)} \mathbf{U}^{(M,i)} \quad \mathbf{A}^{(1)} \mathbf{U}^{(M,i)} \right),$$

where $\mathbf{P}_0^p$ is a projection matrix of the FEM basis functions from order p to the lowest order 0, $\mathbf{U}^{(M,i)}$ is the $\mathbf{U}^M$ obtained in (20) for the ith direction. The stability constant $\alpha_{LB} = \lambda_{min} \min\left(1, \frac{\omega}{\omega'}\right)$ is obtained from the smallest eigenvalue of an eigenvalue problem [21, p. 56], which, in practice, is only performed once for smallest frequency of interest ω'.

In the on-line stage, we evaluate

$$\|\hat{\boldsymbol{r}}_i(\omega)\|_{Y^{(hp)}}^2 = \left(\left(\mathbf{w}^{(i)}(\omega)\right)^H \mathbf{G}^{(i,i)} \left(\mathbf{w}^{(i)}(\omega)\right) \right)^{1/2},$$

$$\|\hat{\boldsymbol{r}}_i(\omega) - \hat{\boldsymbol{r}}_j(\omega)\|_{Y^{(hp)}}^2 = \left(\|\hat{\boldsymbol{r}}_i(\omega)\|_{Y^{(hp)}}^2 + \|\hat{\boldsymbol{r}}_j(\omega)\|_{Y^{(hp)}}^2 - 2\text{Re}\left(\left(\mathbf{w}^i(\omega)\right)^H \mathbf{G}^{(i,j)} \left(\mathbf{w}^{(j)}(\omega)\right) \right) \right)^{1/2},$$

for each ω by updating the vector

$$\mathbf{w}^{(i)}(\omega) = \begin{pmatrix} \omega \\ -\mathbf{p}^{M,(i)}(\omega) \\ -\omega \mathbf{p}^{M,(i)}(\omega) \end{pmatrix},$$

where $\mathbf{p}^{M,(i)}$ refers to $\mathbf{p}^M$ for the ith direction. We then apply (30) to obtain the a posteriori error estimate.

5 | SCALING OF THE MPT UNDER PARAMETER CHANGES

Two results that aid the computation of the frequency sweep of an MPT for an object with scaled conductivity and an object with a scaled object size from an already known frequency sweep of the MPT for the same shaped object are stated below.

Lemma 2. *Given the MPT coefficients for an object αB with material parameters μ_r and σ_* at frequency $s\omega$, the coefficients of the MPT for an object, which has the same B, α and μ_r, but with conductivity $s\sigma_*$, at frequency ω, are given by*

$$(\mathcal{M}[\alpha B, \omega, s\sigma_*, \mu_r])_{ij} = (\mathcal{M}[\alpha B, s\omega, \sigma_*, \mu_r])_{ij}, \tag{32}$$

where $(\mathcal{M}[\alpha B, s\omega, \sigma_*, \mu_r])_{ij}$ denote the coefficients of the original MPT at frequency $s\omega$.

Proof. This result immediately follows from (5) and (7) since both are written in terms of $\nu = \alpha^2\sigma_*\mu_0\omega$. ∎

Lemma 3. *Given the MPT coefficients for an object αB with material parameters μ_r and σ_* at frequency $s^2\omega$, the coefficients of the MPT for an object $s\alpha B$, which is the same as B apart from having size $s\alpha$, at frequency ω, are given by*

$$(\mathcal{M}[s\alpha B, \omega, \sigma_*, \mu_r])_{ij} = s^3 \left(\mathcal{M}\left[\alpha B, s^2\omega, \sigma_*, \mu_r\right]\right)_{ij}, \tag{33}$$

where $\left(\mathcal{M}\left[\alpha B, s^2\omega, \sigma_*, \mu_r\right]\right)_{ij}$ denote the coefficients of the original MPT at frequency $s^2\omega$.

Proof. For the case of $\mu_r = 1$ this result was proved by Ammari et al.[15] We generalize this to $0 < \mu_r < \mu_r^{max} < \infty$ as follows: We use the splitting $(\mathcal{M})_{ij} := \left(\mathcal{N}^0\right)_{ij} - (C^{\sigma_*})_{ij} + \left(\mathcal{N}^{\sigma_*}\right)_{ij}$ presented in Reference 5 and let $\theta_{i,B}^{(0)}$ denote the solution to (6). Then, we find that

$$\frac{1}{s}\theta_{i,sB}^{(0)}\left(s\xi'\right) = \theta_{i,B}^{(0)}\left(\xi'\right),$$

where $\theta_{i,sB}^{(0)}$ is the solution to (6) with B replaced by sB. If $\theta_{i,B}^{(1)}\left[s^2\nu\right]$ is the solution to (7) with ν replaced by $s^2\nu$, then, we find that

$$\frac{1}{s}\theta_{i,sB}^{(1)}[\nu]\left(s\xi'\right) = \theta_{i,B}^{(1)}\left[s^2\nu\right]\left(\xi'\right),$$

where $\theta_{i,sB}^{(1)}[\nu]$ is the solution to (7) with B replaced by sB. Using the above, the definitions in lemma 1 of Reference 5, and $\xi = s\xi'$ we find

$$\left(C^{\sigma_*}\left[\alpha\left(sB\right), \omega, \sigma_*, \mu_r\right]\right)_{ij} = -\frac{i\alpha^3\nu}{4}\int_{sB} e_i \cdot \left(\xi \times \left(\theta_{i,sB}^{(1)}[\nu] + \theta_{i,sB}^{(0)}\right)\right)d\xi$$

$$= \frac{is^3\alpha^3\nu}{4}\int_B e_i \cdot \left(s\xi' \times \left(\theta_{i,sB}^{(1)}[\nu]\left(s\xi'\right) + \theta_{i,sB}^{(0)}\left(s\xi'\right)\right)\right)d\xi'$$

$$= \frac{is^3\alpha^3\left(s^2\nu\right)}{4}\int_B e_i \cdot \left(\xi' \times \left(\theta_{i,B}^{(1)}\left[s^2\nu\right] + \theta_{i,B}^{(0)}\right)\right)d\xi' = s^3\left(C^{\sigma_*}\left[\alpha B, s^2\omega, \sigma_*, \mu_r\right]\right)_{ij},$$

$$\left(\mathcal{N}^0\left[\alpha\left(sB\right), \mu_r\right]\right)_{ij} = \frac{\alpha^3}{2}\left[\tilde{\mu}^{-1}\right]_\Gamma \int_{sB} e_i \cdot \nabla_\xi \times \theta_{i,sB}^{(0)}d\xi$$

$$= \frac{s^3\alpha^3}{2}\left[\tilde{\mu}^{-1}\right]_\Gamma \int_B e_i \cdot \frac{1}{s}\nabla_{\xi'} \times \left(s\theta_{i,B}^{(0)}\right)d\xi' = s^3\left(\mathcal{N}^0\left[\alpha B, \mu_r\right]\right)_{ij},$$

$$\left(\mathcal{N}^{\sigma_*}\left[\alpha\left(sB\right), \omega, \sigma_*, \mu_r,\right]\right)_{ij} = \frac{\alpha^3}{2}\left[\tilde{\mu}^{-1}\right]_\Gamma \int_{sB} e_i \cdot \nabla_\xi \times \theta_{i,sB}^{(1)}[\nu]d\xi$$

$$= \frac{s^3\alpha^3}{2}\left[\tilde{\mu}^{-1}\right]_\Gamma \int_B e_i \cdot \frac{1}{s}\nabla_{\xi'} \times \left(s\theta_{i,B}^{(1)}\left[s^2\nu\right]\right)d\xi' = s^3\left(\mathcal{N}^{\sigma_*}\left[\alpha B, s^2\omega, \sigma_*, \mu_r,\right]\right)_{ij},$$

and the result immediately follows. ∎

6 | NUMERICAL EXAMPLES OF PODP

The PODP algorithm has been implemented in the Python interface to the high order finite element solver `NGSolve` package led by the group of Schöberl[23,24,27] available at `https://ngsolve.org`. The snapshots are computed by solving (9) and (11) using `NGSolve` and their H(curl) conforming tetrahedral finite element basis functions of order p on meshes of spacing h.[26] Following the solution of (16), and the application of (13), the coefficients of $\mathcal{M}[\alpha B, \omega]$[3] follow by simple postprocessing of (5). If desired, PODP output certificates can also be efficiently computed using the approach described in Section 4.3. The Python scripts for the computations presented can be accessed at `https://github.com/BAWilson94/MPT-Calculator`. Specifically, the results presented were obtained with version 6.2.1905 of `NGSolve` and commit number 17d5b33208 of `MPT-Calculator`.

---

[3]In the following, when presenting numerical results for the PODP, we frequently choose to drop the superscript PODP on $\mathcal{M}[\alpha B, \omega]$ $\mathcal{R}[\alpha B, \omega]$, $\mathcal{I}[\alpha B, \omega]$ and $\mathcal{N}^0[B]$, introduced in Section 4.3, for brevity of presentation where no confusion arises. Also, we will return to using the notation $\mathcal{M}[\alpha B, \omega, \mu_r, \sigma_*]$, which illustrates the full parameter dependence, in Section 7 when considering scaling of conductivity and object size.

6.1 | Conducting permeable sphere

We begin with the case where $B_\alpha = \alpha B$ is a permeable conducting sphere of radius $\alpha = 0.01$ m and B is the unit sphere centered at the origin. The sphere is chosen to have a relative permeability $\mu_r = 1.5$ and conductivity $\sigma_* = 5.96 \times 10^6$ S/m. To produce the snapshots of the full order model, we set Ω to be a ball 100 times the radius of B^4, generate a mesh of 26,385 unstructured tetrahedra, refined toward the object, and apply $p = 3$ elements. We have chosen this discretization since it has already been found to produce an accurate representation of $\mathcal{M}[\alpha B, \omega]$ for $10^2 < \omega < 10^8$ rad/s by comparing with exact solution of the MPT for a sphere.[3,44] Indeed, provided that the geometry discretization error is under control, performing p-refinement of the full order model solution results in exponential convergence to the true solution.[1] For this mesh, p-refinement has been found to give exponential convergence of $\mathcal{M}[\alpha B, \omega]$ down to relative error of less than 0.01% and so further increases in the size of Ω were not deemed to be required.

We follow two different schemes for choosing frequencies ω for generating the solution vectors $\mathbf{q}(\omega)$ required for $\mathbf{D}$ in (18). Firstly, we consider linearly spaced frequencies $\omega_{min} \leq \omega_n \leq \omega_{max}$, $n = 1, 2, \ldots, N$, where, as in Section 4.1, N is the number of representative full order solution snapshots that follow from using each value of ω_n, in turn, and denote this choice of samples by "Lin" in the results. Secondly, we consider logarithmically spaced frequencies $\omega_{min} \leq \omega_n \leq \omega_{max}$ and denote this regime by "Log" in the results.

Considering both linearly and logarithmically spaced frequencies with $\omega_{min} = 1 \times 10^2$ rad/s, $\omega_{max} = 1 \times 10^8$ rad/s and $N = 9, 13, 17$, in turn, to generate the snapshots, the application of an SVD to $\mathbf{D}$ in (19) leads to the results shown in Figure 3 where the values have been scaled by σ_1 and are strictly decreasing. We observe that "Log" case produces singular values σ_i/σ_1, which tend to 0 with increasing i, while the "Lin" case produces σ_i/σ_1, which tend to a finite constant with increasing i. Also shown is the tolerance $TOL = 1 \times 10^{-3}$, that is, we define M such that $\sigma_M/\sigma_1 \leq TOL < \sigma_{M+1}/\sigma_1$ and create the matrices $\mathbf{U}^M$, $\mathbf{\Sigma}^M$, and $(\mathbf{V}^M)^H$ by taking the first M columns of $\mathbf{U}$, M rows of $\mathbf{V}^H$ and first M rows and columns of $\mathbf{\Sigma}$.

The superior performance of logarithmically spaced frequencies over those linearly spaced is illustrated in Figure 4 using the error measure $|e(\Lambda_i(\omega))| := |\Lambda_i^{exact}(\omega) - \Lambda_i^{PODP}(\omega)|/|\Lambda_i^{exact}(\omega)|$ with ω, where $\Lambda_i(\omega) = \lambda_i(\mathcal{R}[\alpha B, \omega] + \mathcal{N}^0[\alpha B]) + i\lambda_i(\mathcal{I}[\alpha B, \omega])$ and $\lambda_i(\cdot)$ indicates the ith eigenvalue. We see that choosing ω_n to be logarithmically spaced for the representative full order model solution snapshots results in a smaller error compared with choosing ω_n to be linear spaced and also shows an algebraic increase with ω for $N > 5$.
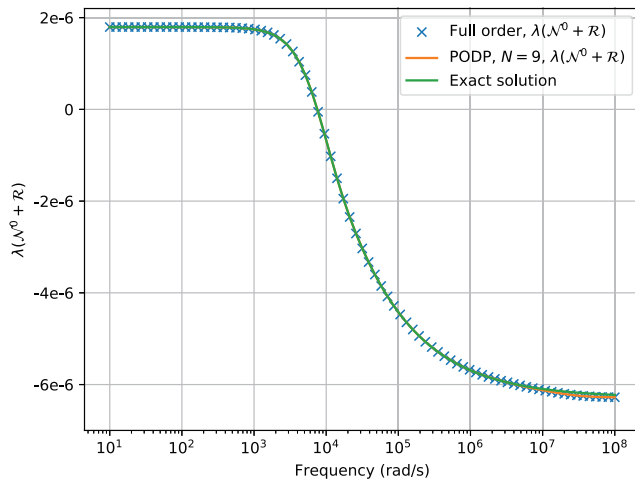

(A) Linearly spaced ω_n (B) Logarithmically spaced ω_n
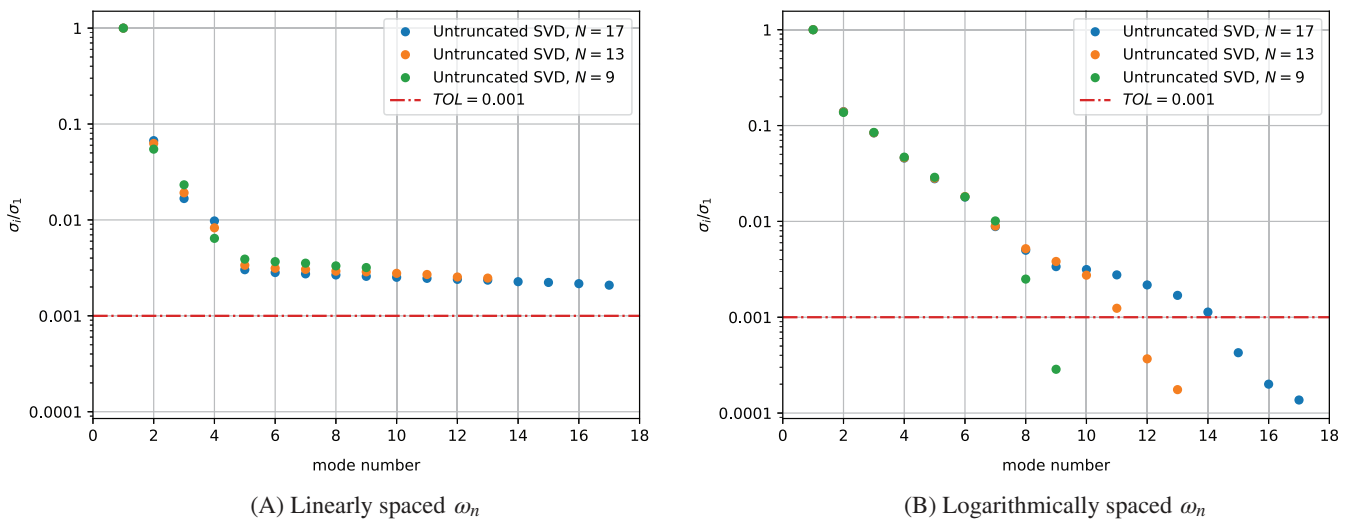
FIGURE 3 Sphere with $\mu_r = 1.5$, $\sigma_* = 5.96 \times 10^6$ S/m, $\alpha = 0.01$ m: PODP applied to the computation of $\mathcal{M}[\alpha B, \omega]$ showing σ_i/σ_1 for (A) linearly spaced ω_n and (B) logarithmically spaced ω_n

---

[4]Loosely speaking, given the decay of the solutions to (6) and (7), this truncation is such that the difference between the continuous solutions on the bounded and unbounded domains is not more than 1%, but typically much smaller in practice.
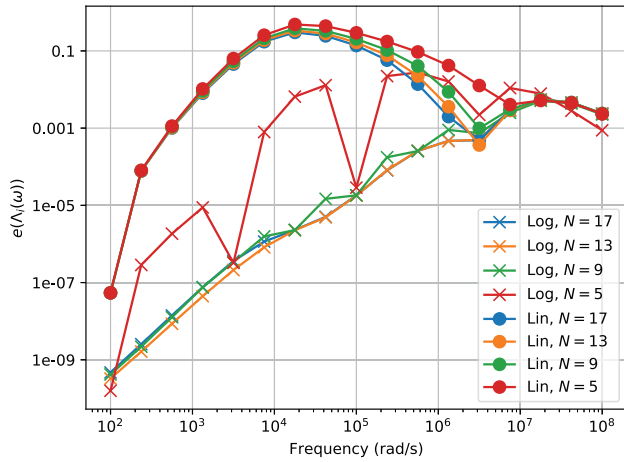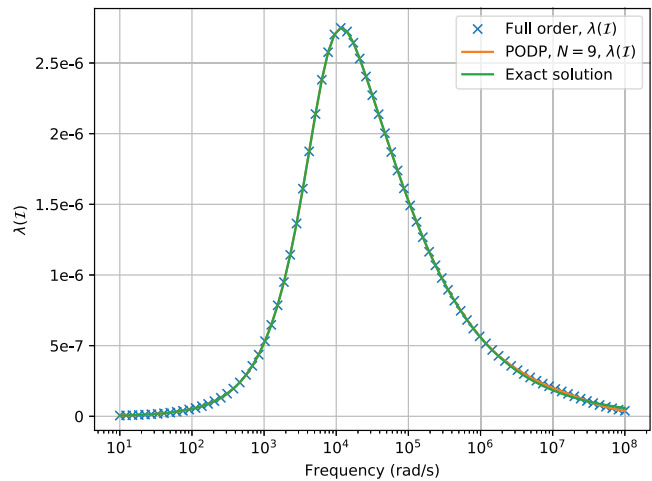
FIGURE 4 Sphere with $\mu_r = 1.5$, $\sigma_* = 5.96 \times 10^6$ S/m, $\alpha = 0.01$ m: PODP applied to the computation of $\mathcal{M}[\alpha B, \omega]$ showing variation of $e(\Lambda_i(\omega))$ with ω for linearly and logarithmically spaced frequencies

**(A)** $\lambda_i(\mathcal{N}^0[\alpha B] + \mathcal{R}[\alpha B, \omega])$

(B) $\lambda_i(\mathcal{I}[\alpha B, \omega])$

FIGURE 5 Sphere with $\mu_r = 1.5$, $\sigma_* = 5.96 \times 10^6$ S/m, $\alpha = 0.01$ m: PODP applied to the computation of $\mathcal{M}[\alpha B, \omega]$ using $N = 9$ and $TOL = 1 \times 10^{-4}$ showing (A)$\lambda_i\left(\mathcal{N}^0[\alpha B] + \mathcal{R}[\alpha B, \omega]\right)$ and (B)$\lambda_i(\mathcal{I}[\alpha B, \omega])$ each with ω

Further tests reveal that the accuracy of the PODP using $N = 9, 13, 17$ and logarithmically spaced ω_n remains similar to that shown in Figure 4 for $TOL \leq 1 \times 10^{-3}$ for this problem. Next, we show in Figure 5 a comparison of $\lambda_i(\mathcal{R}[\alpha B, \omega])$ and $\lambda_i(\mathcal{I}[\alpha B, \omega])$, each with ω, for the full order model, PODP using $N = 9$ and the exact solution. Again, the results for $i = 1, 2, 3$ are identical and, hence, only $i = 1$ is shown. In this figure, we observe excellent agreement between PODP, the full order model solution and exact solution.

In Figure 6, we show the certification of the output $\left(\mathcal{R}^{\mathrm{PODP}}[\alpha B, \omega] + \mathcal{N}^{0,\mathrm{PODP}}[\alpha B]\right)_{ii} \pm (\Delta[\omega])_{ii}$ (summation of repeated indices is not implied) and $\left(\mathcal{I}^{\mathrm{PODP}}[\alpha B, \omega]\right)_{ii} \pm (\Delta[\omega])_{ii}$, each with ω, obtained using the a posteriori error estimate in Lemma 1 and computed using the technique described in Section 4.3 for the case where $i = 1$ and with $N = 17, 21$ and $TOL = 1 \times 10^{-6}$. Similar certification can be obtained for the other tensor coefficients. We observe the output certification is almost indistinguishable from the the MPT coefficients obtained with PODP for low frequencies in both cases and the error estimates rapidly tend to 0 for all ω as N is increased. Note that the a posteriori error bounds always vanish when ω corresponds to an ω_n used for the representative full order solution snapshots. The larger error estimates for higher frequencies indicate that the MPT coefficients obtained by PODP for these frequencies is less reliable than those for smaller frequencies. However, smaller error bounds and increased reliability is achieved by increasing N as shown in Figure 6(C) and 6(D) compared with Figure 6(A) and 6(B). Alternatively, smaller error bounds and increased reliability can be achieved by choosing the additional ω_n for the representative offline solution snapshots corresponding to where $(\Delta[\omega])_{ij}$ is largest[45] and, if desired, this could be used as part of an adaptive process in a similar manner to Reference 21. Note that $TOL = 1 \times 10^{-6}$ is chosen as larger tolerances lead to larger error estimates; however, this reduction in tolerance does not substantially affect the computational cost of the ROM. Although
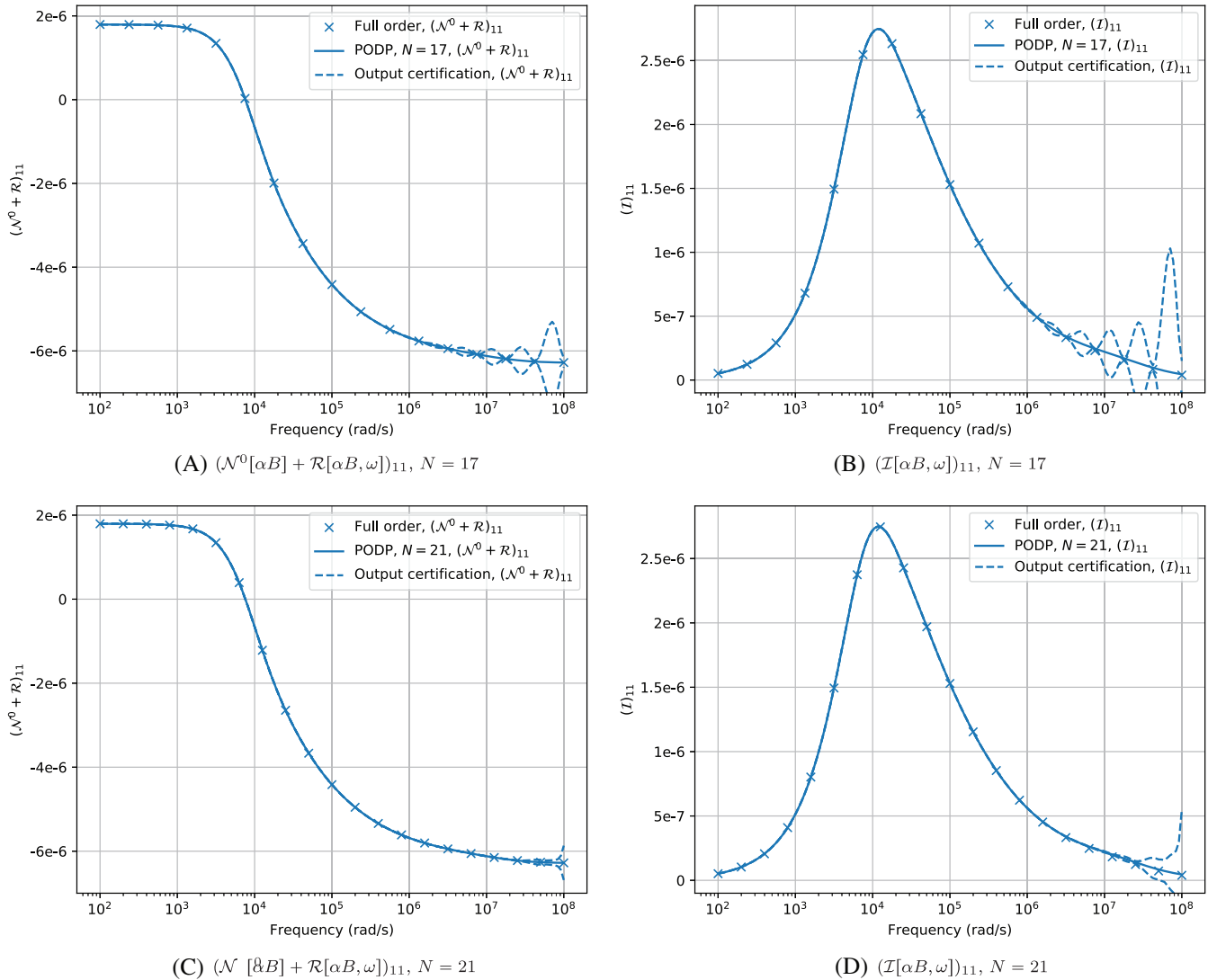
FIGURE 6 Sphere with $\mu_r = 1.5$, $\sigma_* = 5.96 \times 10^6$ S/m, $\alpha = 0.01$ m: PODP applied to the computation of $\mathcal{M}[\alpha B, \omega]$ with $TOL = 1 \times 10^{-6}$ showing the PODP solution, full order model solutions and certification of the output $(\cdot) \pm (\Delta[\omega])_{11}$ for (A)$\left(\mathcal{N}^0[\alpha B] + \mathcal{R}[\alpha B, \omega]\right)_{11}$ using $N = 17$, (B)$(\mathcal{I}[\alpha B, \omega])_{11}$ using $N = 17$, (C)$\left(\mathcal{N}^0[\alpha B] + \mathcal{R}[\alpha B, \omega]\right)_{11}$ using $N = 21$ and (D)$(\mathcal{I}[\alpha B, \omega])_{11}$ using $N = 21$, each with ω

the effectivity indices $(\Delta[\omega])_{11}/|\left(\mathcal{R}[\alpha B, \omega] - \mathcal{R}^{\text{PODP}}[\alpha B, \omega]\right)_{11}|$ and $(\Delta[\omega])_{11}/|\left(\mathcal{I}[\alpha B, \omega] - \mathcal{I}^{\text{PODP}}[\alpha B, \omega]\right)_{11}|$) of the PODP with respect to the full order model are clearly larger at higher frequencies, we emphasize that they are computed at negligible additional cost, they converge rapidly to the MPT coefficients obtained with PODP as N is increased and give credibility in the PODP solution without the need of performing additional full order model solutions to validate the ROM.

The computational speed-ups offered by using the PODP compared with a frequency sweep performed with the full order model are shown in Figure 7(A) where $N = 9, 13, 17$ and logarithmically spaced ω_n are chosen with $\omega_{min} = 1 \times 10^2$ rad/s, $\omega_{max} = 1 \times 10^8$ rad/s, as before. For the comparison, we vary the number of output points N_0 produced in a frequency sweep and measure the time taken to produce each of these frequency sweeps using a 2.9 GHz quad core Intel i5 processor and also show the percentage speed up offered by each of these PODP sweeps. Shown in Figure 7(B) is the breakdown of the computational time for the offline and online stages of the PODP for the case where $N = 13$. Note, in particular, that the computational cost increases very slowly with N_0 and that the additional cost involved in computing the output certification is small. The breakdown of computational costs for other N is similar. The implementation in NGSolve and in the MPT-calculator tool is parallelized and further reductions in time can be achieved by increasing the number of cores used. In particular, in NGSolve parallelism is exploited in many aspects, which include meshing, matrix assembly, linear algebra and iterative solution of the linear systems, and is further exploited in MPT-calculator through the computation of the representative full order model solution snapshots, computation of the ROM solutions at different output frequencies, computation of the PODP MPT coefficients and calculation of the a posteriori errorestimate.
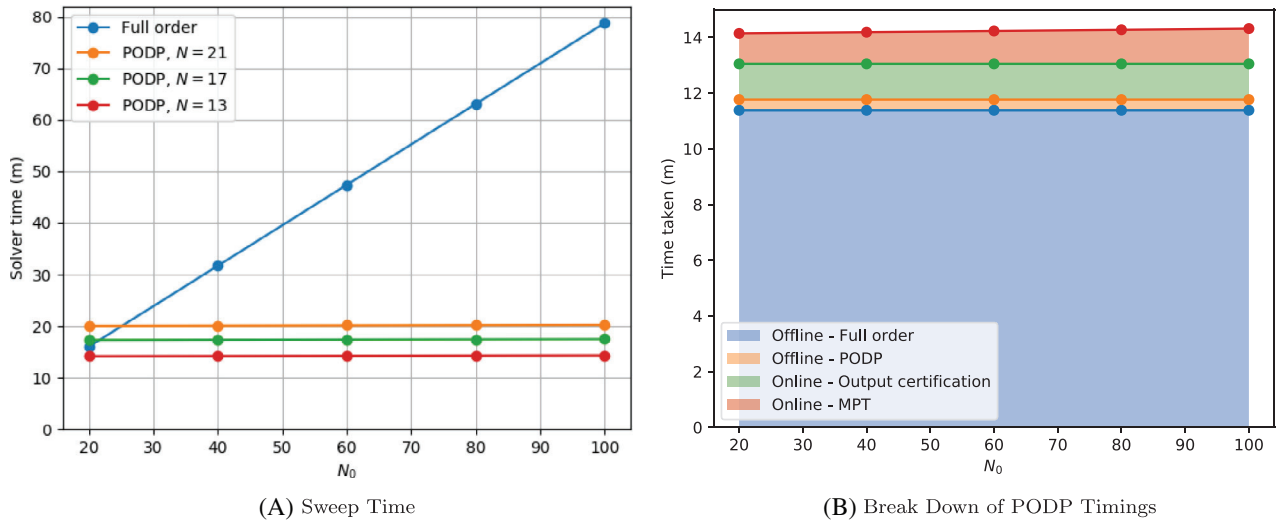
FIGURE 7 Sphere with $\mu_r = 1.5$, $\sigma_* = 5.96 \times 10^6$ S/m, $\alpha = 0.01$ m: PODP applied to the computation of $\mathcal{M}[\alpha B, \omega]$ with $TOL = 1 \times 10^{-6}$ showing, for different numbers of outputs N_0, (A) sweep computational time for $N = 13, 17, 21$ compared with full order and (B) a typical breakdown of the offline and online computational times for $N = 13$

6.2 | Conducting permeable torus

Next, we consider $B_\alpha = \alpha B$ to be a torus where B has major and minor radii $a = 2$ and $b = 1$, respectively, $\alpha = 0.01$ m and the object is permeable and conducting with $\mu_r = 1.5$, $\sigma_* = 5 \times 10^5$ S/m. The object is centered at the origin so that it has rotational symmetry around the e_1 axis, therefore, $\mathcal{M}[\alpha B, \omega]$ has independent coefficients $(\mathcal{M}[\alpha B, \omega])_{11}$ and $(\mathcal{M}[\alpha B, \omega])_{22} = (\mathcal{M}[\alpha B, \omega])_{33}$, and, thus, $\mathcal{N}^0[\alpha B]$, $\mathcal{R}[\alpha B, \omega]$ and $\mathcal{I}[\alpha B, \omega]$ each have two independent eigenvalues for each ω. Hence, there are only two independent curves for $\lambda_i\left(\mathcal{N}^0[\alpha B] + \mathcal{R}[\alpha B, \omega]\right)$ and $\lambda_i(\mathcal{I}[\alpha B, \omega])$, as functions of ω. To compute the full order model, we set Ω to be a sphere of radius 100, centered at the origin and containing B, generate a mesh of 26,142 unstructured tetrahedra, refined toward the object, and apply $p = 3$ elements. This discretization has already been found to produce an accurate representation of $\mathcal{M}[\alpha B, \omega]$ for the frequency range with $\omega_{min} = 1 \times 10^2$ rad/s and $\omega_{max} = 1 \times 10^8$ rad/s with the full order model.

The reduced order model is constructed using $N = 13$ representative full order solution snapshots that follow from using each value of the logarithmically spaced ω_n in turn and $TOL = 1 \times 10^{-4}$. Figure 8 shows the results for $\lambda_i\left(\mathcal{N}^0[\alpha B] + \mathcal{R}[\alpha B, \omega]\right)$ and $\lambda_i(\mathcal{I}[\alpha B, \omega])$, each with ω, for both the full order model and the PODP. The agreement is excellent in both cases.

In Figure 9 we show the certification of the output $\left(\mathcal{R}^{PODP}[\alpha B, \omega] + \mathcal{N}^{0,PODP}[\alpha B]\right)_{ii} \pm (\Delta[\omega])_{ii}$ (no summation over repeated indices implied) and $\left(\mathcal{I}^{PODP}[\alpha B, \omega]\right)_{ii} \pm (\Delta[\omega])_{ii}$, each with ω, obtained using the a posteriori error estimate in Lemma 1 and computed using the technique described in Section 4.3 for the case where $N = 17$ and $TOL = 1 \times 10^{-6}$. Note that we increased the number of snapshots from $N = 13$ to $N = 17$ and have reduced the tolerance to ensure a small error estimate.

## 6.3 | Conducting permeable tetrahedron

The third object considered is where $B_\alpha = \alpha B$ is a conducting permeable tetrahedron. The vertices of the tetrahedron B are chosen to be at the locations

$$v_1 = \begin{pmatrix} 0 \\ 0 \\ 0 \end{pmatrix}, \quad v_2 = \begin{pmatrix} 7 \\ 0 \\ 0 \end{pmatrix}, \quad v_3 = \begin{pmatrix} 5.5 \\ 4.6 \\ 0 \end{pmatrix}, \quad \text{and} \quad v_4 = \begin{pmatrix} 3.3 \\ 2 \\ 5 \end{pmatrix},$$

the object size is $\alpha = 0.01$ m and the tetrahedron is permeable and conducting with $\mu_r = 2$ and $\sigma_* = 5.96 \times 10^6$ S/m. The object does not have rotational or reflectional symmetries, therefore, $\mathcal{M}[\alpha B, \omega]$ has six independent coefficients and,
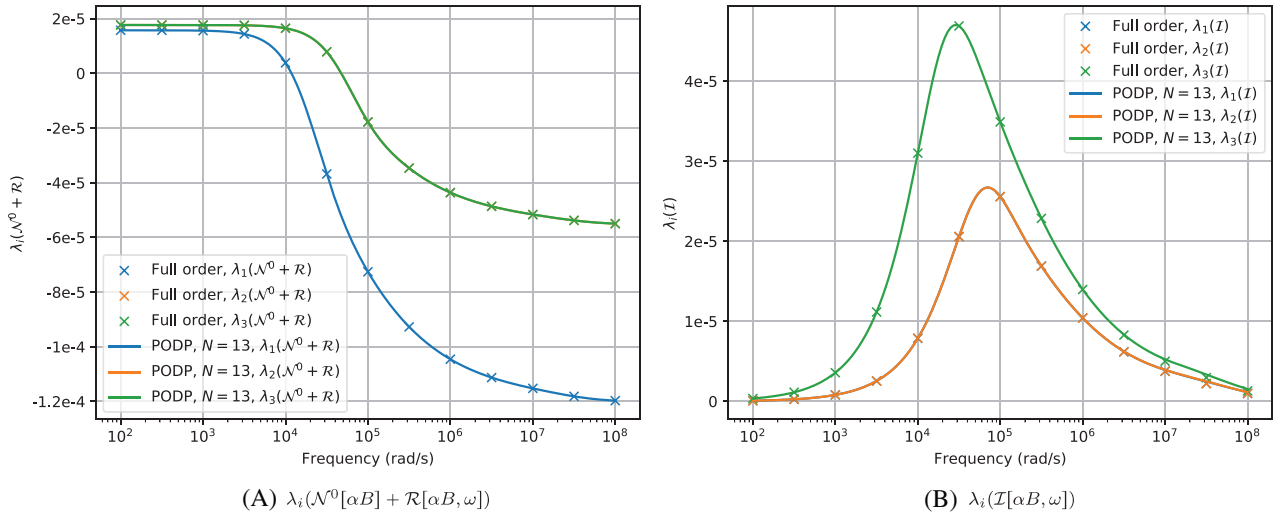
FIGURE 8 Torus with major and minor radii of $a = 2$ and $b = 1$, respectively, and $\mu_r = 1.5$, $\sigma_* = 5 \times 10^5$ S/m, $\alpha = 0.01$ m: PODP applied to the computation of $\mathcal{M}[\alpha B, \omega]$ using $N = 13$ and $TOL = 1 \times 10^{-4}$ showing (A)$\lambda_i\left(\mathcal{N}^0[\alpha B] + \mathcal{R}[\alpha B, \omega]\right)$ and (B)$\lambda_i(\mathcal{I}[\alpha B, \omega])$, each with ω
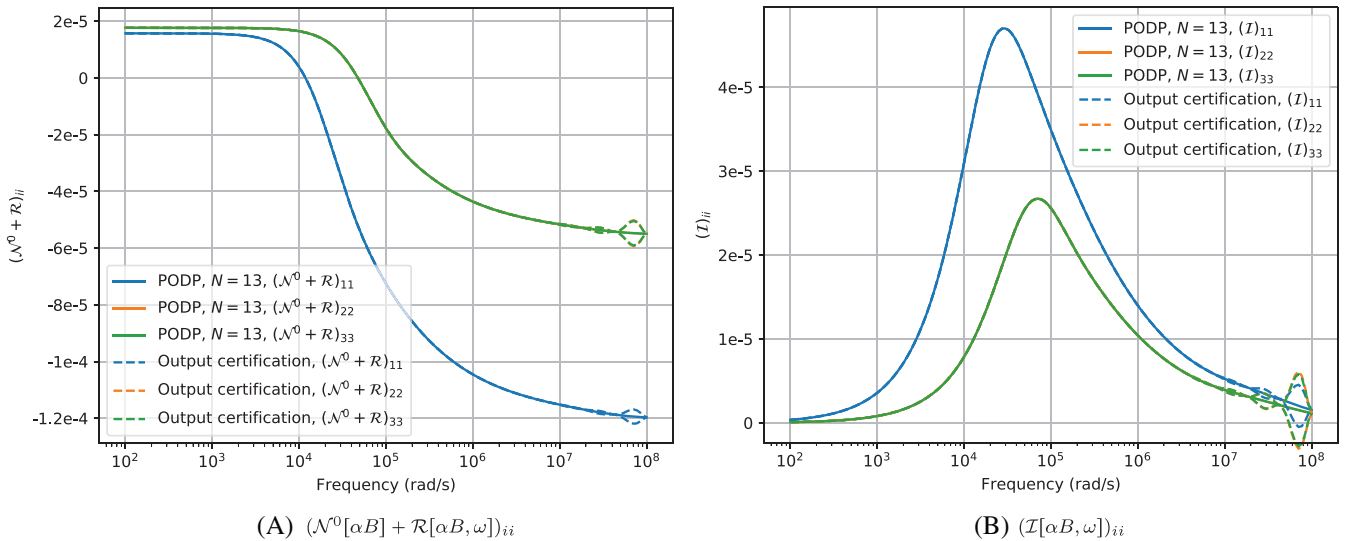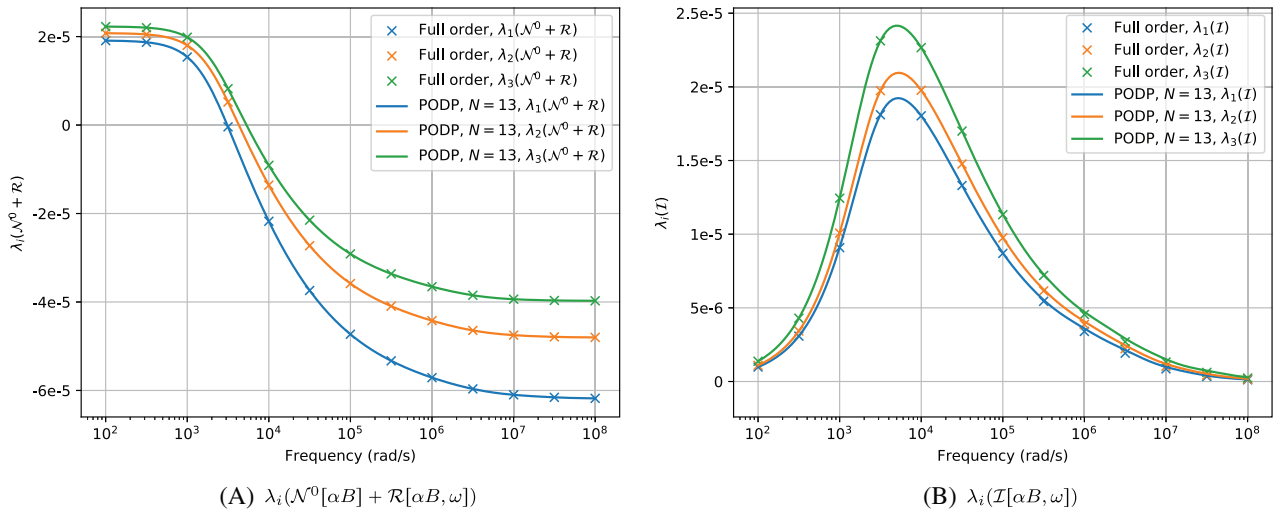

FIGURE 9 Torus with $\mu_r = 1.5$, $\sigma_* = 5 \times 10^5$ S/m, $\alpha = 0.01$ m: PODP applied to the computation of $\mathcal{M}[\alpha B, \omega]$ using $TOL = 1 \times 10^{-6}$ and $N = 17$ showing the PODP solution and certification of the output $(\cdot) \pm (\Delta[\omega])_{ii}$ for (A)$\left(\mathcal{N}^0[\alpha B] + \mathcal{R}[\alpha B, \omega]\right)_{ii}$, (B)$(\mathcal{I}[\alpha B, \omega])_{ii}$, each with ω
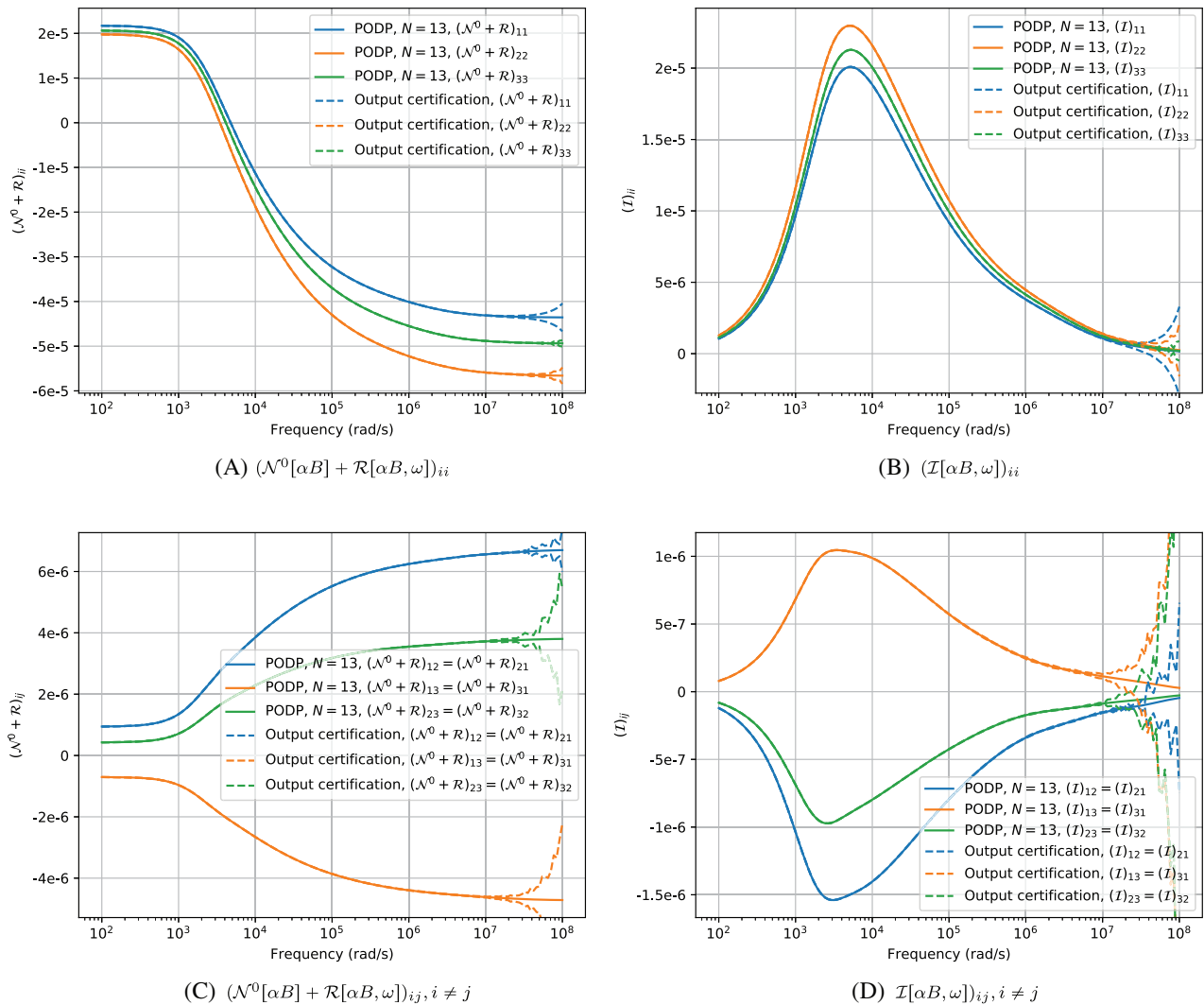
thus, $\mathcal{N}^0[\alpha B]$, $\mathcal{R}[\alpha B, \omega]$ and $\mathcal{I}[\alpha B, \omega]$ each have three independent eigenvalues for each ω. To compute the full order model, we set Ω to be a cube with sides of length 200 centered about the origin, generate a mesh of 21,427 unstructured tetrahedra, refined toward the object, and apply $p = 3$ elements. This discretization has already been found to produce an accurate representation of $\mathcal{M}[\alpha B, \omega]$ for the frequency range with $\omega_{min} = 1 \times 10^2$ rad/s and $\omega_{max} = 1 \times 10^8$ rad/s.

The reduced order model is constructed using $N = 13$ representative full order solution snapshots that follow from using each value of the logarithmically spaced ω_n in turn and $TOL = 1 \times 10^{-4}$. Figure 10 shows the results for $\lambda_i\left(\mathcal{N}^0[\alpha B] + \mathcal{R}[\alpha B, \omega]\right)$ and $\lambda_i(\mathcal{I}[\alpha B, \omega])$, each with ω, for both the full order model and the PODP. The agreement is excellent in both cases.

In Figure 11 we show the certification of the output $\left(\mathcal{R}^{PODP}[\alpha B, \omega] + \mathcal{N}^{0,PODP}[\alpha B]\right)_{ij} \pm (\Delta[\omega])_{ij}$ and $\left(\mathcal{I}^{PODP}[\alpha B, \omega]\right)_{ij} \pm (\Delta[\omega])_{ij}$, both with ω, for $i = j$ and $i \neq j$ obtained using the a posteriori error estimate in Lemma 1 and computed using the technique described in Section 4.3 for the case where $N = 21$ and $TOL = 1 \times 10^{-6}$. Once again, we increased the number of snapshots from $N = 13$ to $N = 21$ and have reduced the tolerance to ensure tight certificates bounds, except at large frequencies.

(A) $\lambda_i(\mathcal{N}^0[\alpha B] + \mathcal{R}[\alpha B, \omega])$

(B) $\lambda_i(\mathcal{I}[\alpha B, \omega])$

FIGURE 10 Irregular tetrahedron with $\mu_r = 2$, $\sigma_* = 5.96 \times 10^6$ S/m, $\alpha = 0.01$ m: PODP applied to the computation of $\mathcal{M}[\alpha B, \omega]$ using $N = 13$ and $TOL = 1 \times 10^{-4}$ showing (A)$\lambda_i\left(\mathcal{N}^0[\alpha B] + \mathcal{R}[\alpha B, \omega]\right)$ and (B)$\lambda_i\left(\mathcal{I}[\alpha B, \omega]\right)$, each with ω

(A) $(\mathcal{N}^0[\alpha B] + \mathcal{R}[\alpha B, \omega])_{ii}$

(B) $(\mathcal{I}[\alpha B, \omega])_{ii}$

(C) $(\mathcal{N}^0[\alpha B] + \mathcal{R}[\alpha B, \omega])_{ij}, i \neq j$

(D) $\mathcal{I}[\alpha B, \omega])_{ij}, i \neq j$

FIGURE 11 Irregular tetrahedron with $\mu_r = 2$, $\sigma_* = 5.96 \times 10^6$ S/m, $\alpha = 0.01$ m: PODP applied to the computation of $\mathcal{M}[\alpha B, \omega]$ using $TOL = 1 \times 10^{-6}$ and $N = 21$ showing the PODP solution and certification of the output $(\cdot) \pm (\Delta[\omega])_{ij}$ for (A)$\left(\mathcal{N}^0[\alpha B] + \mathcal{R}[\alpha B, \omega]\right)_{ij}$, $i = j$(B)$(\mathcal{I}[\alpha B, \omega])_{ij}, i = j$, (C)$\left(\mathcal{N}^0[\alpha B] + \mathcal{R}[\alpha B, \omega]\right)_{ij}, i \neq j$, (D)$(\mathcal{I}[\alpha B, \omega])_{ij} i \neq j$, each with ω
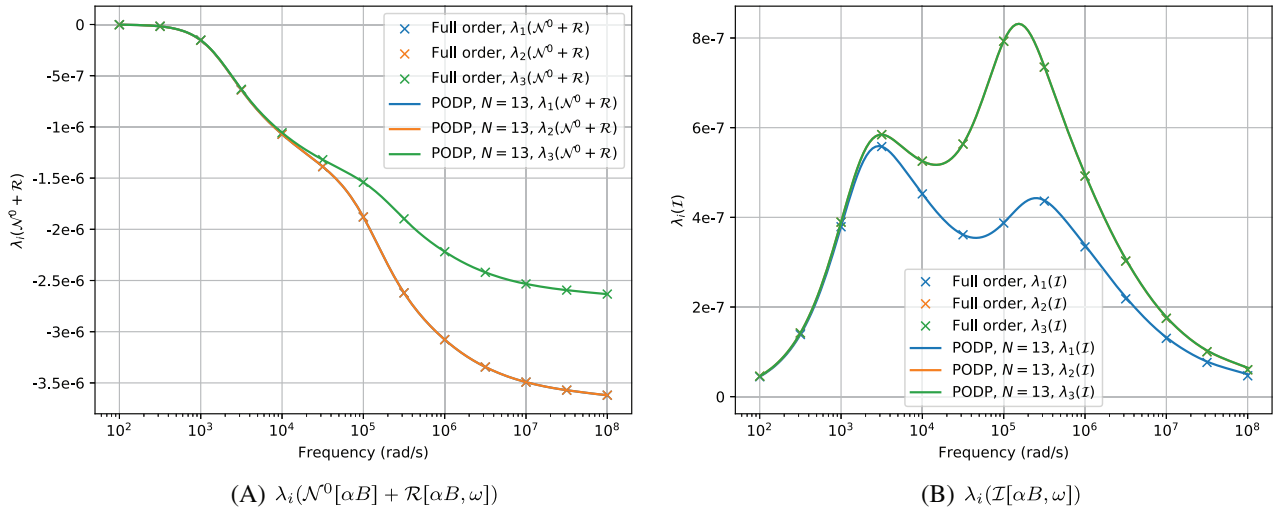
FIGURE 12   Inhomogeneous bar with two distinct conductivities (see section 6.1.3 of Reference 16): PODP applied to the computation of $\mathcal{M}[\alpha B, \omega]$ using $N = 13$ and $TOL = 1 \times 10^{-4}$ showing (A)$\lambda_i\left(\mathcal{N}^0[\alpha B] + \mathcal{R}[\alpha B, \omega]\right)$ and (B)$\lambda_i(\mathcal{I}[\alpha B, \omega])$, each with ω.

6.4 | Inhomogeneous conducting bar

As a final example we consider $B_\alpha = \alpha B$ to be the inhomogeneous conducting bar made up from two different conducting materials. The size, shape and materials of this object are the same as those presented in section 6.1.3 of Reference 16. This object has rotational and reflectional symmetries such that $\mathcal{M}[\alpha B, \omega]$ has independent coefficients $(\mathcal{M}[\alpha B, \omega])_{11}$, $(\mathcal{M}[\alpha B, \omega])_{22} = (\mathcal{M}[\alpha B, \omega])_{33}$ and, thus, $\mathcal{N}^0[\alpha B]$, $\mathcal{R}[\alpha B, \omega]$ and $\mathcal{I}[\alpha B, \omega]$ each have two independent eigenvalues for each ω. To compute the full order model, we set Ω to be a sphere of radius 100, centered about the origin, generate a mesh of 30,209 unstructured tetrahedra, refined toward the object, and apply $p = 3$ elements. This discretization has already been found to produce an accurate representation of $\mathcal{M}[\alpha B, \omega]$ for the frequency range with $\omega_{min} = 1 \times 10^2$ rad/s and $\omega_{max} = 1 \times 10^8$ rad/s.

The reduced order model is constructed using $N = 13$ representative full order solution snapshots that follow from using each value of the logarithmically spaced ω_n in turn and $TOL = 1 \times 10^{-4}$. Figure 12 shows the results for $\lambda_i\left(\mathcal{N}^0[\alpha B] + \mathcal{R}[\alpha B, \omega]\right)$ and $\lambda_i(\mathcal{I}[\alpha B, \omega])$, each with ω, for both the full order model and the PODP. The agreement is excellent in both cases. The behavior of $\lambda_i\left(\mathcal{N}^0[\alpha B] + \mathcal{R}[\alpha B, \omega]\right)$ with ω for the inhomogeneous conducting bar is different to that for a homogeneous object, showing the presence of multiple nonlocal points of inflection rather being sigmoid with ω. Similarly, $\lambda_i(\mathcal{I}[\alpha B, \omega])$, for the inhomogeneous conducting bar, shows the presence of local maxima rather than a single maxima. For further details about the behavior of MPT spectral signature of inhomogeneous objects we refer to Reference 16.

In Figure 13 we show the output certificates $\left(\mathcal{R}^{PODP}[\alpha B, \omega] + \mathcal{N}^{0,PODP}[\alpha B]\right)_{ii} \pm (\Delta[\omega])_{ii}$ (no summation over repeated indices implied) and $\left(\mathcal{I}^{PODP}[\alpha B, \omega]\right)_{ii} \pm (\Delta[\omega])_{ii}$, both with ω, obtained using the a posteriori error estimates in Lemma 1 and computed using the technique described in Section 4.3 for the case where $N = 23$ and $TOL = 1 \times 10^{-6}$. Note that we increased the number of snapshots from $N = 13$ to $N = 23$ and have reduced the tolerance to ensure small error estimates, except at large frequencies.
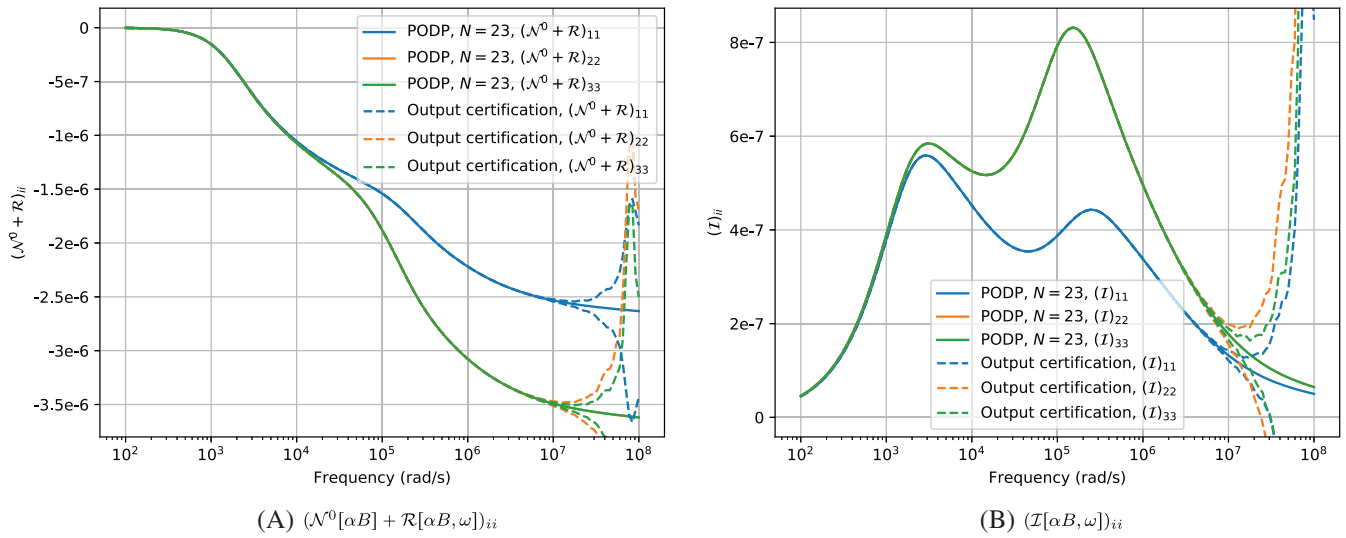
7 | NUMERICAL EXAMPLES OF SCALING

In this section we illustrate the application of the results presented in Section 5.

7.1 | Scaling of conductivity

As an illustration of Lemma 2, we consider a conducting permeable sphere $B_\alpha = \alpha B$ where $\alpha = 0.01$ m with materials properties $\mu_r = 1.5$ and $\sigma_*^{(1)} = 1 \times 10^7$ S/m and a second object, which is the same as the first except that

(A) $(\mathcal{N}^0[\alpha B] + \mathcal{R}[\alpha B, \omega])_{ii}$ (B) $(\mathcal{I}[\alpha B, \omega])_{ii}$

FIGURE 13 Inhomogeneous bar with two distinct conductivities (see section 6.1.3 of Reference 16): PODP applied to the computation of $\mathcal{M}[\alpha B, \omega]$ using $N = 23$ showing the PODP solution and certification of the output $(\cdot) \pm (\Delta[\omega])_{ii}$ for (A)$\left(\mathcal{N}^0[\alpha B] + \mathcal{R}[\alpha B, \omega]\right)_{ii}$, (B)$(\mathcal{I}[\alpha B, \omega])_{ii}$, each with ω
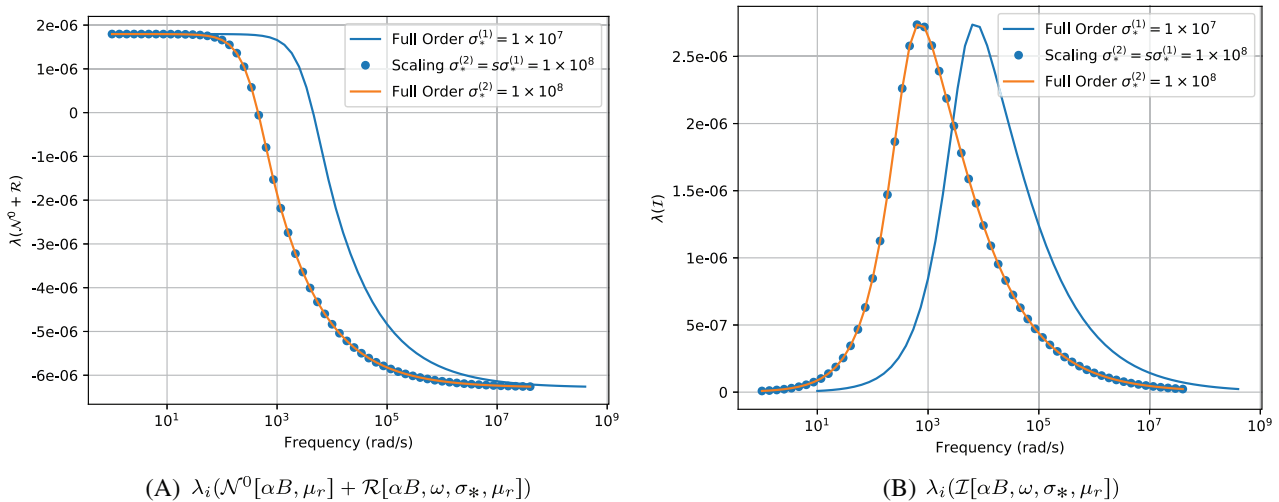
(A) $\lambda_i(\mathcal{N}^0[\alpha B, \mu_r] + \mathcal{R}[\alpha B, \omega, \sigma_*, \mu_r])$ (B) $\lambda_i(\mathcal{I}[\alpha B, \omega, \sigma_*, \mu_r])$

FIGURE 14 Sphere with $\mu_r = 1.5$, $\sigma_*^{(1)} = 1 \times 10^7$ S/m, $\alpha = 0.01$ m and second sphere, which is the same as the first except that $\sigma_*^{(2)} = s\sigma_*^{(1)} = 10\sigma_*^{(1)}$: showing the translation predicted by (32) compared with the full order model solutions for (A)$\lambda_i\left(\mathcal{N}^0[\alpha B, \mu_r] + \mathcal{R}[\alpha B, \omega, \sigma_*, \mu_r]\right)$ and (B)$\lambda_i(\mathcal{I}[\alpha B, \omega, \sigma_*, \mu_r])$

$\sigma_*^{(2)} = s\sigma_*^{(1)} = 10\sigma_*^{(1)}$. In Figure 14, we compare the full order computations of $\mathcal{M}\left[\alpha B, \omega, \sigma_*^{(1)}, \mu_r\right]$ and $\mathcal{M}\left[\alpha B, \omega, \sigma_*^{(2)}, \mu_r\right]$ with that obtained from (32). We observe that the translation predicted by (32) is in excellent agreement with the full order model solution for $\mathcal{M}\left[\alpha B, \omega, \sigma_*^{(2)}, \mu_r\right]$.

7.2 | Scaling of object size

To illustrate Lemma 3, we consider a conducting permeable tetrahedron $B_\alpha^{(1)} = \alpha^{(1)}B = 0.01B$ with vertices as described in Section 6.3 and material properties $\mu_r = 1.5$ and $\sigma_* = 1 \times 10^6$ S/m. Then, we consider a second object $B_\alpha^{(2)} = \alpha^{(2)}B = s\alpha^{(1)}B = 0.015B$, which, apart from its size, is otherwise the same as $B_\alpha^{(1)}$. In Figure 15, we compare the full order computations of $\mathcal{M}\left[\alpha^{(1)}B, \omega, \sigma_*, \mu_r\right]$ and $\mathcal{M}\left[\alpha^{(2)}B, \omega, \sigma_*, \mu_r\right]$ with that obtained from (33). We observe that the translation and scaling predicted by (33) is in excellent agreement with the full order model solution for $\mathcal{M}\left[\alpha^{(2)}B, \omega, \sigma_*, \mu_r\right]$.
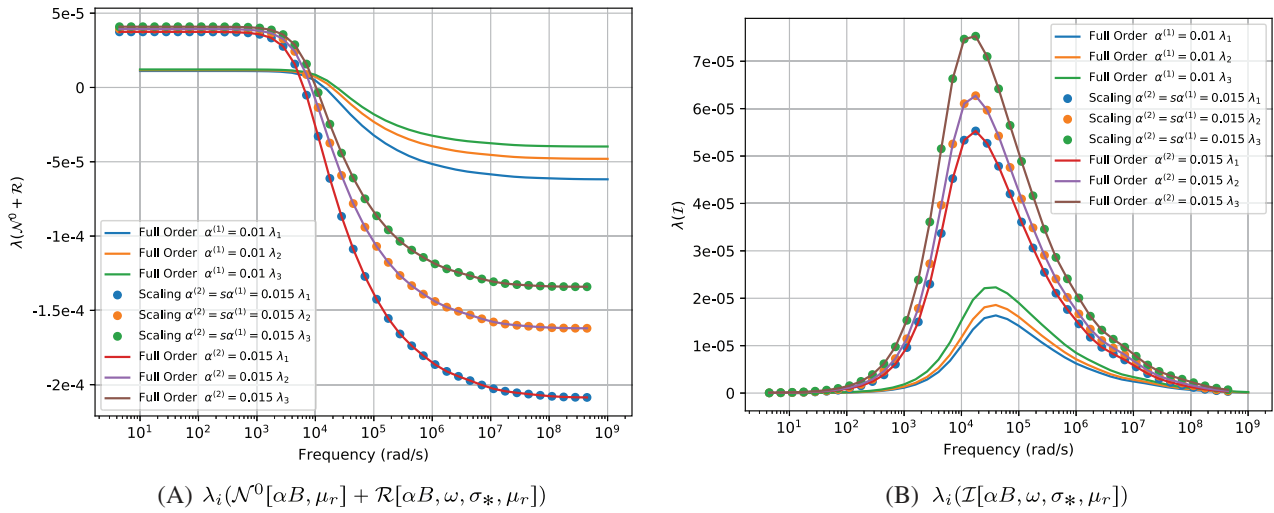
FIGURE 15 Tetrahedron $B_\alpha^{(1)} = \alpha^{(1)} B = 0.01 B$ with $\mu_r = 1.5$ and $\sigma_* = 1 \times 10^6$ S/m, $\alpha = 0.01$ m and a second tetrahedron, which is the same as the first except that $B_\alpha^{(2)} = \alpha^{(2)} B = s\alpha^{(1)} B = 0.015 B$: showing the translation and scaling predicted by (33) compared with the full order model solutions for (A)$\lambda_i \left(\mathcal{N}^0 [\alpha B, \mu_r] + \mathcal{R} [\alpha B, \omega, \sigma_*, \mu_r] \right)$ and (B)$\lambda_i \left(\mathcal{I} [\alpha B, \omega, \sigma_*, \mu_r] \right)$

8 | CONCLUSIONS

An application of a ROM using PODP for the efficient computation of the spectral signature of the MPT has been studied in this article. The MPT coefficients follow from computing solutions to a vectorial transmission problem, which has been approximated by a high order $\boldsymbol{H}$ (curl) conforming discretization using the `NGSolve` finite element package and we called this the full order model. The offline stage of the ROM involves computing a small number representative full order solution snapshots at logarithmically spaced frequencies, then, in the online stage, the spectral signature of the MPT is rapidly and accurately predicted to arbitrarily fine fidelity using PODP. An a posteriori error estimate for the MPT coefficients obtained with PODP, with respect to those obtained with the full order model, has been derived. This can be computed for a small additional computational cost during the online stage of the ROM allowing the PODP prediction of the MPT coefficients to be certified and check their accuracy is within acceptable limits. If desired, this error estimate could be used to drive an adaptive procedure for choosing new snapshots, in a similar manner to the presented approach in Reference 21. However, by choosing the frequency snapshots logarithmically, accurate spectral signatures of the MPT were already obtained with small error bounds. In addition, simple scaling results, which enable the MPT spectral signature to be easily computed from an existing set of coefficients under the scaling of an object's conductivity or object size, have been derived. This has been implemented in the parallelized `MPT-Calculator` software tool, available at `https://github.com/BAWilson94/MPT-Calculator`. A series of numerical examples have been presented to demonstrate the accuracy and efficiency of our approach for homogeneous and inhomogeneous conducting permeable objects. Future work involves applying the presented approach to generate a dictionary of MPT spectral signatures for different objects, enabling larger dictionaries to be obtained in less time and with increased accuracy, for the purpose of improved metallic object identification using a (machine learning) classifier.

CONFLICT OF INTEREST
This paper does not have any conflicts of interest.

DATA AVAILABILITY STATEMENT

ORCID

Paul D. Ledger 🔟 https://orcid.org/0000-0002-2587-7023

REFERENCES

1. Ledger PD, Lionheart WRB. Characterising the shape and material properties of hidden targets from magnetic induction data. *IMA J Appl Math*. 2015;80(6):1776-1798.
2. Ammari H, Chen J, Chen Z, Garnier J, Volkov D. Target detection and characterization from electromagnetic induction data. *J Math Pure Appl*. 2014;101(1):54-75.
3. Ledger PD, Lionheart WRB. An explicit formula for the magnetic polarizability tensor for object characterization. *IEEE Trans Geosci Remote Sens*. 2018;56(6):3520-3533.
4. Ledger PD, Lionheart WRB. The spectral properties of the magnetic polarizability tensor for metallic object characterisation. *Math Methods Appl Sci*. 2020;43:78-113.
5. Ledger PD, Lionheart WRB. Understanding the magnetic polarizability tensor. *IEEE Trans Magn*. 2016;52(5):6201216.
6. Rehim OAA, Davidson JL, Marsh LA, O'Toole MD, Armitage D, Peyton AJ. Measurement system for determining the magnetic polarizability tensor of small metallic targets. Paper presented at: Proceedings of the IEEE Sensor Application Symposium. Zadar, Croatia; 2015.
7. Davidson JL, Rehim OAA, Hu P, Marsh LA, O'Toole MD, Peyton AJ. On the magnetic polarizability of us coinage. *Meas Sci Technol*. 2018;29:035501.
8. Makkonen J, Marsh LA, Vihonen J, et al. Knn classification of metallic targets using the magnetic polarizability tensor. *Meas Sci Technol*. 2014;25:055105.
9. Makkonen J, Marsh LA, Vihonen J, et al. Improving the reliability for classification of metallic targets using a wtmd portal. *Meas Sci Technol*. 2015;26:105103.
10. Rehim OAA, Davidson JL, Marsh LA, O'Toole MD, Peyton AJ. Magnetic polarizability spectroscopy for low metal anti-personnel mine surrogates. *IEEE Sens J*. 2016;16:3775-3783.
11. Zhao Y, Yin W, Ktistis C, Butterworth D, Peyton AJ. On the low-frequency electromagnetic responses of in-line metal detectors to metal contaminants. *IEEE Trans Instrum Meas*. 2014;63:3181-3189.
12. Zhao Y, Yin W, Ktistis C, Butterworth D, Peyton AJ. Determining the electromagnetic polarizability tensors of metal objects during in-line scanning. *IEEE Trans Instrum Meas*. 2016;65:1172-1181.
13. Karimian N, O'Toole MD, Peyton AJ. Electromagnetic tensor spectroscopy for sorting of shredded metallic scrap. Paper presented at: Proceedings of the IEEE SENSORS 2017 Conference; 2017; Glasgow, UK: IEEE.
14. Ledger PD, Lionheart WRB. Generalised magnetic polarizability tensors. *Math Methods Appl Sci*. 2018;41:3175-3196.
15. Ammari H, Chen J, Chen Z, Volkov D, Wang H. Detection and classification from electromagnetic induction data. *J Comput Phys*. 2015;301:201-217.
16. Ledger PD, Lionheart WRB, Amad AAS. Characterisation of multiple conducting permeable objects in metal detection by polarizability tensors. *Math Methods Appl Sci*. 2019;42(3):830-860.
17. van Verre W, Özdeğer T, Gupta A, Podd FJW, Peyton AJ. Threat identification in humanitarian demining using machine learning and spectroscopic metal detection. Paper presented at: Proceedings of the International Conference on Intelligent Data Engineering and Automated Learning (IDEAL); 2019:542-549; Springer, New York, NY.
18. Marsh LA, Ktistis C, Järvi A, Armitage DW, Peyton AJ. Determination of the magnetic polarizability tensor and three dimensional object location for multiple objects using a walk-through metal detector. *Meas Sci Technol*. 2014;25:055107.
19. Hiptmair R. Boundary element methods for eddy current computation. *Boundary Element Analysis (Lecture Notes in Applied and Computational Mechanics Book Series Vol. 29)*. New York, NY: Springer; 2007:213-248.
20. Hiptmair R, Ostrowski J. Coupled boundary-element scheme for eddy-current computation. *J Eng Math*. 2005;51:231-250.
21. Hesthaven JS, Rozza G, Stamm B. *Certified Reduced Basis Methods for Parametrized Partial Differential Equations*. New York, NY: Springer; 2016.
22. Seoane M, Ledger PD, Gil AJ, Zlotnik S, Mallett M. A combined reduced order-full order methodology for the solution of 3D magneto-mechanical problems with application to MRI scanners. *Int J Numer Methods Eng*. 2020;121:3529-3559.
23. Schöberl J. *C++11 Implementation of Finite Elements in Ngsolve. Technical Report, ASC Report 30/2014*. Vienna, Austria: Institute for Analysis and Scientific Computing, Vienna University of Technology; 2014.
24. Schöberl J. Netgen - an advancing front 2d/3d-mesh generator based on abstract rules. *Comput Vis Sci*. 1997;1(1):41-52.
25. Ledger PD, Zaglmayr S. hp-finite element simulation of three-dimensional eddy current problems on multiply connected domains. *Comput Methods Appl Mech Eng*. 2010;199:3386-3401.
26. Schöberl J, Zaglmayr S. High order Nédélec elements with local complete sequence properties. *COMPEL Int J Comput Math Electr Electron Eng*. 2005;24(2):374-384.
27. Zaglmayr S. *High Order Finite Elements for Electromagnetic Field Computation* [PhD thesis]. Johannes Kepler University Linz; 2006.

28. Niroomandi S, Alfaro I, Cueto E, Chinesta F. Model order reduction for hyperelastic materials. *Int J Numer Methods Eng*. 2010;81(9):1180-1206.

29. Radermacher A, Reese S. POD-based model reduction with empirical interpolation applied to nonlinear elasticity. *Int J Numer Methods Eng*. 2016;107(6):477-495.

30. Wang Y, Yu B, Cao Z, Zou W, Yu G. A comparative study of POD interpolation and POD projection methods for fast and accurate prediction of heat transfer problems. *Int J Heat Mass Transf*. 2012;55(17-18):4827-4836.

31. Bialecki RA, Kassab AJ, Fic A. Proper orthogonal decomposition and modal analysis for acceleration of transient FEM thermal analysis. *Int J Numer Methods Eng*. 2005;62(6):774-797.

32. Luo Z, Du J, Xie Z, Guo Y. A reduced stabilized mixed finite element formulation based on proper orthogonal decomposition for the non-stationary Navier–Stokes equations. *Int J Numer Methods Eng*. 2011;88(1):31-46.

33. Pettit CL, Beran PS. Application of proper orthogonal decomposition to the discrete Euler equations. *Int J Numer Methods Eng*. 2002;55(4):479-497.

34. Kerler-Back J, Stykel T. Model reduction for linear and nonlinear magneto-quasistatic equations. *Int J Numer Methods Eng*. 2017;111(13):1274-1299.

35. Chatterjee A. An introduction to the proper orthogonal decomposition. *Curr Sci*. 2000;78(7):808–817.

36. Ammari H, Buffa A, Nédélec J-C. A justification of eddy currents model for the Maxwell equations. *SIAM J Appl Math*. 2000;60(5):1805-1823.

37. Soleimani M, Lionheart WRB, Peyton AJ, Ma X, Higson SR. A three-dimensional inverse finite-element method applied to experimental eddy-current imaging data. *IEEE Trans Magn*. 2006;42:1560-1567.

38. Brown BM, Marletta M, Reyes Gonzales J. Uniqueness for an inverse problem in electromagnetism with partial data. *J Differ Equ*. 2016;260(8):6525-6547.

39. Ngsolve. https://ngsolve.org. Accessed October 8, 2020.

40. Abdi H, Williams LJ. Principal component analysis. *Wiley Interdiscipl Rev Comput Stat*. 2010;2(4):433-459.

41. Bjorck A. *Numerical Methods for Least Squares Problems*. Philadelphia, PA: SIAM; 1996.

42. Hansen PC. *Rank-Deficient and Discrete Ill-Posed Problems: Numerical Aspects of Linear Inversion*. Philadelphia, PA: SIAM; 2005.

43. Golub GH, van Loan CF. *Matrix Computations*. Baltimore: John Hopkins University Press; 1996.

44. Wait JR. A conducting sphere in a time varying magnetic field. *Geophsics*. 1951;16(4):666-672.

45. Wilson BA. *In preparation* [PhD thesis]. Swansea University; 2021.